


RESEARCH ARTICLE

The vortex structure and near-surface winds of Typhoon *Faxai* (2019) during landfall. Part II: Evaluation of WRF simulations

Takuya Takahashi^{1,2}  | David S. Nolan¹  | Brian D. McNoldy¹ 

¹Rosenstiel School of Marine,
Atmospheric, and Earth Science,
University of Miami, Miami, Florida USA

²Atmosphere and Ocean Department,
Japan Meteorological Agency, Tokyo,
Japan

Correspondence

Takuya Takahashi, Rosenstiel School of
Marine, Atmospheric, and Earth Science,
University of Miami, Miami, FL, USA.
Email: ttakahashi@earth.miami.edu

Abstract

This two-part study presents a comprehensive analysis of (1) the vortex structure, (2) the inner core planetary boundary layer (PBL) wind profile, and (3) the overland surface winds of Typhoon *Faxai*(2019) during landfall observationally (Part I) and in high-resolution Weather Research and Forecasting Model (WRF) simulations (Part II). Part II presents a framework for evaluating the wind field in the WRF simulations of Typhoon *Faxai* (2019) by comparing them with the observations presented in Part I. First, WRF simulations with two different surface roughness z_0 tables are presented. The simulation with the default z_0 table in WRF is shown to largely overestimate the surface wind speed. The overestimation is largely mitigated by using larger z_0 based on the climatology for urban and forest areas in Japan. Next, using the modified z_0 table, WRF simulations with three different PBL parametrizations, namely, Mellor–Yamada–Janjić, Yonsei University, and Mellor–Yamada–Nakanishi–Niino schemes are presented, and their impacts on the simulated vortex structure, inner core PBL wind profile, and overland surface winds are evaluated. In particular, the simulated surface winds are in good agreement with the observations outside the inner core of Typhoon *Faxai*. However, during the passage of the eyewall, the maximum surface winds are underestimated in the simulations. We show that the underestimation of the inertial stability, associated with the excessively large inner core of Typhoon *Faxai* in the simulations, led to the overestimation of the eyewall PBL jet height. This, in turn, caused the underestimation of the peak surface winds, as based on the empirical model of the wind reduction factor $F_{2\text{km}}$ proposed in Part I.

KEYWORDS

boundary layer, NWP, radar, tropical cyclones, winds

1 | INTRODUCTION

1.1 | Background and motivation

The accuracy of numerical forecasts of tropical cyclones (TCs) has improved significantly with the increase in spatial resolution and the improvements in model physics. In particular, past studies confirmed that strong TCs can

be represented far more precisely with the grid spacing as fine as several kilometers (Fierro et al., 2009; Gopalakrishnan et al., 2011; Kanada & Wada, 2016; Nolan et al., 2009a, 2009b). It has been established that the choice of planetary boundary layer (PBL) turbulence closure schemes and the tuning of parameters have first-order impacts on the intensity and size of numerically simulated TCs (e.g., Kanada & Wada, 2016; Zhang et al., 2015).

Significant progress has been made in recent years in the model physics of ocean surface enthalpy and momentum exchange, together with turbulent mixing properties in the PBL under hurricane-force wind conditions (e.g., Donelan et al., 2004; Curcic & Haus, 2020; Chen & Bryan, 2021; Chen & Bryan, 2021; Sroka & Emanuel, 2021). A long history of active research has revealed much of the dynamical and thermodynamical structure and the turbulent mixing characteristics of TC boundary layers (TCBLs) over the ocean through both observational (e.g., Powell, 1982; Franklin et al., 2003; Zhang et al., 2011a) and theoretical (e.g., Eliassen & Lystad, 1977; Shapiro, 1983; Kepert, 2001; Kepert & Wang, 2001; Smith & Vogl, 2008) studies. Both the vortex structure over the PBL and the PBL wind profiles at landfall have been studied using either single- or dual-Doppler radar analyses (e.g., Lee et al., 2000; Shimada et al., 2018; Alford et al., 2020; Biggerstaff et al., 2021; Cha & Bell, 2021). The PBL wind profiles have been explored both observationally and theoretically (e.g., Vickery et al., 2009; Smith & Montgomery, 2013), and compared with the simulated PBL wind profiles (Kepert, 2012).

Many studies have shown that the combination of land terrain, enhanced surface drag, and reduced enthalpy flux after landfall impacts both the structure of the TC vortex and near-surface winds (Kuwagata and Kondo, 1992; Mashiko, 2008; Wu et al., 2009), while the dynamical decay of the TC vortex and the PBL and surface wind characteristics are the topic of current active research both theoretically (e.g., Chen & Chavas, 2020, 2021) and numerically (e.g., Hlywiak & Nolan, 2021). In particular, the impacts of the surface and PBL parametrizations on the dynamical decay after landfall in real-world settings have rarely been explored despite their crucial importance for accurately simulating strong near-surface winds after TC landfalls. In addition, the dynamical link between observed misoscale TCBL structures that cause near-surface wind streaks and the miso- to mesoscale structures that appear in numerically simulated land-falling TCBLs is a current topic of research (e.g., Kosiba et al., 2013; Nolan et al., 2021a, 2021b; Stern et al., 2021).

Despite the drastic improvements in TC forecast accuracy, point-by-point forecasts of strong winds during landfalls based on numerical models are still not realized. Such deterministic forecasting of strong winds of land-falling TCs could be of great value, especially in coastal and urban areas that are prone to damage from strong winds, such as building collapses and large-scale power outages. There are two clear hurdles toward such point-by-point forecasting, especially in the case of hurricane-force winds. The first hurdle is that, even though the TC forecast accuracy has improved significantly over time, current typical track and intensity forecast errors can still lead to a significant error in local wind forecast. The other hurdle

is that there are very few ground-based validations of numerical forecasts of landfalling TCs with hurricane-force winds (e.g., Lin et al., 2010). To address the second point, recent studies have evaluated over-land wind fields in a high-resolution simulation of landfalling hurricanes. Nolan et al. (2021a, 2021b) analyzed the accuracy of the surface wind fields in Weather Research and Forecasting Model (WRF) simulations of Hurricane *Wilma* (2005) that made landfall in southern Florida using two widely used PBL parametrizations—the Yonsei University (YSU) (Hong et al., 2006) and Mellor–Yamada–Janjić (MYJ) (Janjić, 1990; Mellor & Yamada, 1974, 1982) schemes—by comparing them in detail with ground-based wind observations and vertical wind profiles obtained with radars. Despite the fact that the computations were started 27 hr before landfall and did not assimilate observations except for nudging in the outer domain, the point-to-point comparison produced quantitatively consistent results for high winds. Similarly, Hendricks et al. (2021) studied WRF simulations of the wind fields in the southeastern Florida urban corridor during the passage of Hurricane *Irma* (2017), and they also found examples of good correspondence to local observations.

The companion article Takahashi and Nolan (2023, hereafter, Part I) presents a detailed observational analysis of (1) the vortex structure, (2) inner core PBL wind profiles, and (3) near-surface winds of Typhoon *Faxai* (2019) during the landfall over the Kanto region of Japan. Also, in Part I we present an empirical model of the wind reduction factor $F_{2\text{km}}$ that describes the surface wind speed in terms of the properties of the PBL jets.

In this article (Part II), we present a comprehensive evaluation of the simulated vortex structure, the inner core PBL wind profile, and the overland surface winds in the WRF simulations of Typhoon *Faxai* (2019) based on the comparison with observations presented in Part I. We discuss the impacts of surface roughness and PBL parametrizations on the simulated vortex structure and near-surface wind fields. In particular, the simulated 10 m winds at the Automated Meteorological Data Acquisition System (AMeDAS) stations near the track of *Faxai* are directly compared with the observed 10 m winds, and the dynamical origin of the bias in the simulated 10 m winds is discussed based on the empirical model of the wind reduction factor proposed in Part I.

1.2 | Organization of the article

The article is organized as follows. In Section 2, the simulation settings, initial adjustment procedure through the “vortex bogusing” technique, and the overview

of the surface roughness and PBL parametrizations for the simulations are presented. In Section 3, we present WRF simulations of Typhoon *Faxai* (2019) with two different surface roughness tables and three different PBL parametrizations; namely, YSU, MYJ, and Mellor–Yamada–Nakanishi–Niino (MYNN) schemes (Nakanishi, 2001; Nakanishi & Niino, 2009). The impacts of the surface roughness and PBL parametrizations on (1) the simulated vortex structure, (2) inner core PBL wind profiles, and (3) near-surface winds are evaluated through a detailed comparative analysis between the simulations and observations. We discuss how the inner core vortex structure and the PBL jets are dynamically connected, and how these characteristics impact the peak surface winds. In Section 4, we summarize the results.

2 | NUMERICAL METHOD

2.1 | Simulation settings

We numerically simulated Typhoon *Faxai* (2019) from September 7, 1800 UTC, which is about 26 hr before its landfall over the Kanto region of Japan, until September 9, 0000 UTC, when it moved out into the Pacific Ocean, using the WRF model version 4.2.1 (Skamarock, 2019). The domain geometry, together with the initial wind speed (color shading) on the 11th vertical model level (which roughly corresponds to the top of the marine boundary layer at $z \approx 0.98$ km) is shown in Figure 1. All simulations use the outer domain (D01) and a fixed inner (nested) domain (D02). D01 has 540×684 grid points with 3 km horizontal grid spacing, and D02 has 480×600 grid points with the grid spacing of 1 km. D02 is spawned simultaneously with D01 at 1800 UTC on September 7. The setting of the vertical model levels is the same as the hurricane nature run of Nolan et al. (2013).¹

The initial and boundary conditions for the outer domain are generated from the Global Forecasting System “FNL” analysis. The location, size, and intensity of *Faxai* at the simulation start time are adjusted using the vortex bogusing technique developed by Rappin et al. (2013). Details of the adjustment are provided in Section 2.2.

Convective parametrization is not used in either domain because of the high horizontal resolution. Details of the simulation settings are summarized in Table 1. We applied the analysis nudging technique (Deng et al., 2007) to the outer domain (D01) fields to help keep the simulated

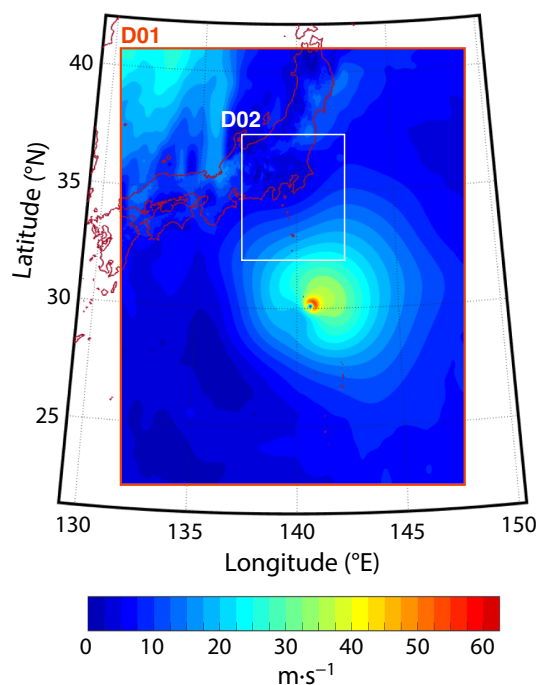


FIGURE 1 The geometry of simulation domains (D01 and D02), superimposed with the initial total horizontal wind speed (color shading) on the 11th vertical model level. [Colour figure can be viewed at wileyonlinelibrary.com]

track close to reality without affecting the inner dynamics of the vortex. Through the nudging procedure, the wind, temperature, and humidity fields in the outer domain are relaxed towards temporally interpolated Global Forecasting System “FNL” analysis fields with the relaxation time of 24 hr. The 24-hr relaxation time is selected through trial and error to enable us to approximate the simulated track during landfall to reality by adjusting the initial vortex location while minimizing the impact on the size and intensity of the vortex.

In the WRF simulations, surface layer schemes diagnose surface winds and momentum fluxes based on the Monin–Obukhov similarity theory (Monin & Obukhov, 1954). The roughness length z_0 over the ocean is obtained following the Charnock relation (Charnock, 1955) with a modification accounting for the leveling off in the high wind regime (Donelan et al., 2004). Over land, z_0 is simply assigned for each land-use type in the surface roughness parametrization.

We performed simulations with different surface roughness length z_0 for each land-use type, as summarized in Table 2.² The first simulation (YSU-W) uses the

¹In our simulations, D01 and D02 share common vertical grid spacings and physical parametrizations. We confirmed that no artifacts related to dynamical inconsistencies arise when the TC center crosses the mesh boundary.

²The surface drag force, which arises from the interaction of air flow with roughness elements of the size $O(1$ m) or smaller, needs to be fully parametrized.

TABLE 1 Specification of simulations.

Dynamical core	Advanced Research WRF v4.2.1
Domain type	Fixed
Grid projection	Lambert conformal
Horizontal resolution	3 km (D01), 1 km (D02)
Time step	12 s (D01), 4 s (D02)
Vertical levels	60
Initial and boundary conditions	Six-hourly Global Forecasting System “FNL” analysis
Convective parametrization	None
Planetary boundary-layer parametrization	Yonsei University (YSU)/Mellor–Yamada–Janjić (MYJ)/Mellor–Yamada–Nakanishi–Niino (MYNN)
Surface layer	Monin–Obukhov similarity scheme
Land surface model	Noah land-surface model
Radiation physics	Rapid radiative transfer model for general circulation models (RRTMG)
Microphysics	Thompson scheme

default roughness length table available with WRF, with the YSU PBL parametrization.³ The second simulation (YSU-J) uses different roughness lengths for urban areas and forests based on the table used for the Japan Meteorological Agency (JMA) non-hydrostatic model (Aoyagi & Seino, 2012). The difference is that z_0 for urban areas and forests is much larger in YSU-J. Next, we performed WRF simulations with MYJ and MYNN PBL parametrizations with the z_0 table used for JMA’s non-hydrostatic model, which we call MYJ-J and MYNN-J respectively.

The results of YSU-W, YSU-J, MYJ-J, and MYNN-J are compared to explore the impacts of the z_0 and PBL parametrizations.

2.2 | Adjustment of the initial location, intensity, and size of the vortex

In order to make the evaluation of simulated surface winds and boundary-layer structure during landfall as accurate as possible, we first went through a trial-and-error process to ensure that the position, intensity, and size of the simulated vortex at landfall are close to reality. In the trial-and-error process, we started simulations with different location, intensity, and size of the initial vortex through the vortex bogusing technique. Before adding in the bogus vortex, the vortex removal is carried out from the initial field created by the WRF Preprocessing System within a specified non-circular filter domain following the method proposed in Kurihara et al. (1993, 1995) to generate the initial environmental fields without a TC vortex. The radial

wind profile of the bogus vortex is prescribed as a modified Rankine vortex at the top of the boundary layer as follows:

$$V(r) = \begin{cases} V_{\max} \left(\frac{r}{\text{RMW}} \right) & (r \leq \text{RMW}) \\ V_{\max} \left(\frac{r}{\text{RMW}} \right)^{-\alpha} & (r > \text{RMW}) \end{cases}, \quad (1)$$

where the maximum wind speed V_{\max} , the radius of maximum wind (RMW), and the decay index α are arbitrary parameters. The altitude of the boundary-layer top is chosen to be 1 km.

In the vertical direction, the wind decays exponentially in the boundary layer down to the surface, whereas above the boundary layer top the wind field is extrapolated following the formulation presented in Moon and Nolan (2010), which is based on the steady-state axisymmetric hurricane model described in the maximum potential intensity theory of Emanuel (1986). In order to accelerate the dynamical adjustment of the bogus vortex within about 6 hr into the simulation through deep convection and establishment of the secondary circulation, the moisture field is artificially enhanced as far as it does not exceed the saturation value following the formulation in Rappin et al. (2013):

$$q_{\text{mod}}(r, z) = q_{\text{orig}}(r, z) \left(1 + E \frac{V(r, z)}{V_{\max}} \right), \quad (2)$$

where q_{orig} and q_{mod} are original and modified moisture fields respectively. The enhancement factor E is an arbitrary parameter.

After this trial-and-error procedure to make the track and intensity at landfall as close to the reality as possible,

³In general, PBL parametrizations are necessary when using a grid spacing of ~ 100 m or larger.

TABLE 2 Roughness length modified for YSU-J.

Land-use type	Roughness length (m)	
	YSU-W	YSU-J
Evergreen needleleaf forest	0.5	2.0
Evergreen broadleaf forest	0.5	2.0
Deciduous needleleaf forest	0.5	2.0
Deciduous broadleaf forest	0.5	2.0
Mixed forests	0.5	3.0
Urban and built-up	0.8	3.0
Low-intensity residential	0.8	3.0
High-intensity residential	0.8	3.0
Industrial or commercial	0.8	3.0

Abbreviations: YSU-J, Yonsei University PBL parametrization using the Japan Meteorological Agency's non-hydrostatic model roughness length; YSU-W, Yonsei University PBL parametrization using WRF's default roughness length.

TABLE 3 Bogus vortex parameters.

Initial latitude, longitude	30.1° N, 140.7° E
V_{\max} (m·s ⁻¹)	40
RMW (km)	18
α	0.95
E	0.2

the center of the bogus vortex is fixed at 30.1° N, 140.7° E, which is slightly different than the JMA best track position of 30.2° N, 140.5° E. The initial location and parameters (i.e., V_{\max} , RMW, α , and E) for the bogus vortex used in the simulations are summarized in Table 3.

2.3 | Overview of the PBL parametrizations for the simulations

Although the finest grid spacing of 1 km in this study is sufficient to represent a wide range of dynamical phenomena in TCs down to the mesoscale, it is still one to two orders of magnitude larger than the large eddies that mix the physical quantities in the turbulent PBLs (e.g., Rotunno et al., 2009; Li & Pu, 2021; Chen & Bryan, 2021). Because of this scale gap, the turbulent mixing of the physical quantities in the PBL needs to be fully parametrized. For the WRF simulations presented here, we used three different PBL parametrization schemes; namely, YSU, MYJ, and MYNN.

The YSU scheme is classified as the first-order, non-local closure, or K -profile parametrization (Hong et al., 2006). It is developed from its predecessor, the medium-range forecast PBL parametrization that was used at the National Centers for Environmental Prediction (Hong & Pan, 1996). As a first-order closure, it does not

solve any prognostic equations for higher order turbulence quantities. The eddy viscosity in the YSU parametrization $K_{m,YSU}$ is based on the diagnosed velocity scale w_s and the height of the PBL h :

$$K_{m,YSU} = kw_s z \left(1 - \frac{z}{h}\right)^p, \quad (3)$$

where $k = 0.4$ is the von Karman constant, z is the vertical location, and $p = 2$ is the shape parameter. As a non-local scheme, the YSU parametrization also includes counter-gradient diffusion due to large eddies and the entrainment flux at the PBL top, which are computed in addition to Equation (3).

On the other hand, the MYJ and MYNN schemes are both classified as a turbulence kinetic energy (TKE)-based local closure. The MYJ parametrization is modified from its predecessor, the Mellor–Yamada “level-2.5” scheme (Mellor & Yamada, 1982) based on the four levels of complexity introduced in Mellor and Yamada (1974), and implemented for numerical weather forecasts by Janjić (1990). In the MYJ scheme, as in the Mellor–Yamada level-2.5 scheme, only the prognostic equation for the TKE is solved among the second-order turbulent quantities for the calculation of the eddy diffusivity. Improvements in the MYJ scheme are that the viscous sublayer is introduced in between the ocean surface layer and the level-2.5 Mellor–Yamada PBL schemes (Janjić, 1994), and the procedures for TKE and the master length scale were made more robust and consistent in the wider ranges of atmospheric conditions (Janjić, 2002).

The eddy viscosity in the MYJ scheme is based on the mixing length method (Prandtl, 1925) as follows:

$$K_{m,MYJ} = lqS_m, \quad (4)$$

where l is the turbulence master length scale, $q = \sqrt{2e}$ is the turbulence velocity scale (e is the TKE), and S_m is the diagnosed stability function. The master length scale l is diagnosed based on the following interpolation formula (Blackadar, 1962):

$$l = l_0 \frac{kz}{kz + l_0}, \quad (5)$$

where the turbulence length scale l_0 is diagnosed as follows:

$$l_0 = \alpha \frac{\int_0^\infty |z|q \, dz}{\int_0^\infty q \, dz}, \quad (6)$$

with the constant α chosen to be 0.3 for the MYJ scheme in WRF v4.2.1.

The MYNN parametrization (Nakanishi, 2001; Nakanishi & Niino, 2009) is also a TKE-based, local closure modified from the Mellor–Yamada closures. The level-2.5 and 3.0 versions of the MYNN scheme are available in WRF v4.2.1. (Olson et al., 2019). The eddy viscosity in MYNN also follows the mixing length formula $K_{m,MYNN} = lqS_m$. We chose the level-2.5 MYNN scheme (MYNN2.5) for the simulation presented here. The MYNN scheme uses a sophisticated “three-layer” harmonic-averaging approach for the calculation of the master length scale: $l^{-1} = l_s^{-1} + l_t^{-1} + l_b^{-1}$, where l_s , l_t , and l_b are the surface layer length, turbulent length, and buoyancy length respectively. The turbulent length l_t is diagnosed based on the same form for l_0 in the MYJ and Mellor–Yamada schemes:

$$l_t = \alpha \frac{\int_0^{z_u} |z|q \, dz}{\int_0^{z_u} q \, dz}. \quad (7)$$

We used the `bl_mynn_mixlength = 1` option, in which the limit of the integration z_u is set to be the height of the PBL top z_i plus the depth of the transition layer δz ($z_u = z_i + \delta z$). Also, an improvement for the calculation of l_b is implemented in the `bl_mynn_mixlength = 1` option making use of a non-local formulation of Bougeault and Lacarrere (1989) known as the “BouLac” length above the PBL top.

For the present simulation, we adopted a modified MYNN PBL scheme following Chen and Bryan (2021). The modified MYNN scheme accounts for the buoyant production of the TKE from surface heat fluxes in the TKE budget at the bottom model level and calculates the master length scale by $l^{-2} = l_s^{-2} + l_t^{-2} + l_b^{-2}$ following a general formula proposed in Mason and Thomson (1992). In addition, for the calculation of the turbulent length l_t , α is changed from 0.23 to 0.1 as in Mellor and Yamada (1974). With these changes, the modified MYNN scheme can produce a logarithmic wind profile near the surface that is more consistent with in-situ observations in hurricanes.

The horizontal TKE advection is neglected for the current simulation (`bl_mynn_tkeadvect = 0`). We note that the recent experimental studies suggest that the inclusion of horizontal TKE advection has effects on the TKE distribution in the eyewall above the PBL and makes the TC inner core slightly smaller (Chen & Bryan, 2021; Wadler et al., 2023). The mass-flux scheme option is also inactivated (`bl_mynn_edmf = 0`).

3 | IMPACTS OF THE SURFACE ROUGHNESS AND PBL PARAMETRIZATION

3.1 | Track and intensity

Figure 2a shows the half-hourly center locations of Typhoon *Faxai* in the simulations (red: YSU-W; blue: YSU-J; magenta: MYJ-J; green: MYNN-J) from September 7, 1800 UTC, to September 9, 0000 UTC. The locations every 3 hr are also shown by the colored circles. The tropical cyclone center location at each time step is determined by a method similar to the “pressure-centroid” method rigorously examined by Nguyen et al. (2014). In addition, the JMA’s best track from September 7, 1800 UTC, to September 9, 0000 UTC, is plotted as a black solid line with square marks. The close-up view during the landfall is shown in Figure 2b. The domain of Figure 2b is denoted by the dashed rectangle in Figure 2a.

The simulated tracks are shifted to the southeast by approximately 10 km before entering Tokyo Bay, but during landfall they are in good agreement with the observed track. We note that from 2000 UTC to 2100 UTC on September 8, the track for MYNN-J deviated to the southeast from the best track by as much as 3 km. *Faxai*’s inner core PBL wind profile is analyzed over Narita Airport in Section 3.3, and its location is shown as a red star in Figure 2b. In addition, 12 AMEDAS observational stations (stations P1 through P12) are selected to directly compare the simulated 10 m wind with observations in Section 3.4, and their locations are shown in Figure 2b as magenta circles. Stations P1 through P12 are the same as those analyzed in Part I. *Faxai*’s inner core winds directly impacted these stations during the landfall.

Figure 3 shows the time evolution of the simulated sea-level pressure at the TC center (Figure 3a) and the maximum 10 m wind (Figure 3b), both obtained from the outputs of the outer domain, along with the best-track values issued by the JMA and Joint Typhoon Warning Center (JTWC). We note that the JMA reports 10-min sustained winds, whereas the JTWC reports 1-min sustained winds for the TC intensity. Typically, the wind-speed values from the WRF outer domain with the horizontal grid spacing

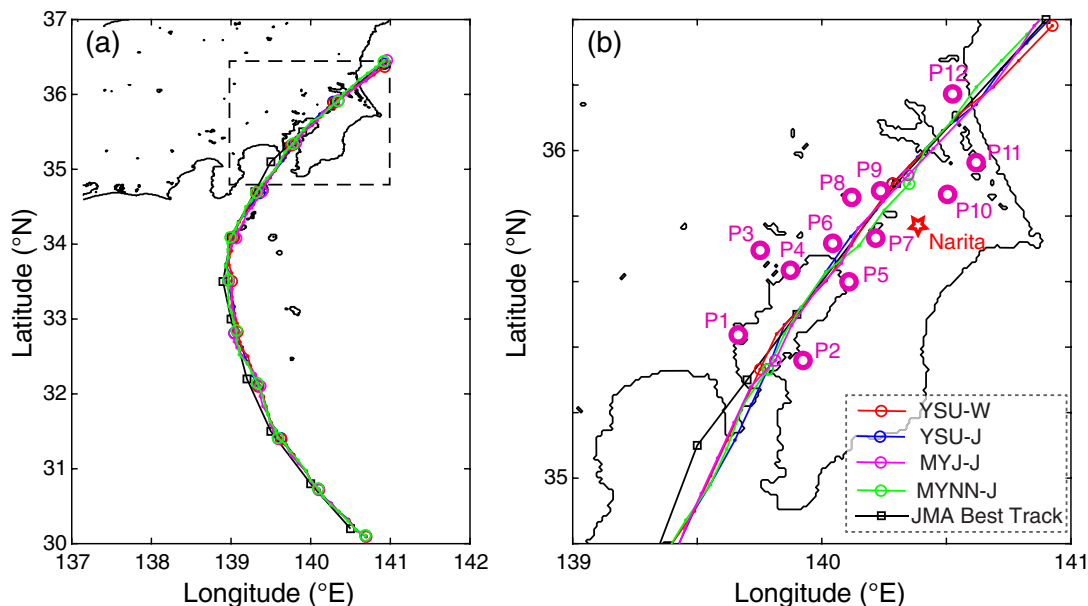


FIGURE 2 The simulated tracks (red: YSU-W; blue: YSU-J; magenta: MYJ-J; green: MYNN-J) and the Japan Meteorological Agency's best track (black solid lines) of Typhoon *Faxai*. (a) The tracks from 1800 UTC on September 7 to 0000 UTC on September 9. The square area encircled by the dashed line in (a) indicates the domain of (b), showing the close-up view during the landfall. The location of the selected surface observational stations (P1 through P12) for point-by-point wind comparison is shown as magenta circles in (b). Also, the location of Narita Airport is shown as a red star mark in (b). YSU-W: Yonsei University PBL parametrization using WRF's default roughness length; YSU/MYJ/MYNN-J: Yonsei University/Mellor–Yamada–Janjić/Mellor–Yamada–Nakanishi–Niino PBL parametrization using the Japan Meteorological Agency's non-hydrostatic model roughness length. [Colour figure can be viewed at wileyonlinelibrary.com]

of 3 km correspond to the wind speed with the averaging time period somewhere in between 1 min and 10 min (e.g., Nolan et al., 2014).

The best-track intensity of *Faxai* reported by the JTWC is significantly higher than the intensity reported by the JMA, particularly during *Faxai*'s peak intensity period (e.g., 0000 UTC on September 8). The discrepancy is greater than the typical difference between the peak 1-min winds and the peak 10-min winds of TCs, which is approximately 10% (Harper et al., 2010). In the western North Pacific, TC intensity analysis relies heavily on the Dvorak technique (Dvorak, 1975, 1984) using geostationary meteorological satellites due to the absence of reconnaissance flights and limited surface observations over the ocean. The discrepancy in the best-track intensity of *Faxai* likely arises, in part, from the differences in both the “current intensity (CI) number” in the Dvorak technique and its conversion to the maximum wind speed. Nakazawa and Hoshino (2009) examined a 20-year operational dataset from 1987, revealing that the CI-numbers reported by the JTWC tend to be slightly higher than those reported by the JMA. For the conversion from the CI-number to maximum wind speed, the JTWC uses the table based on Dvorak (1975), whereas the JMA uses the table based on Koba et al. (1990). For TCs with CI-numbers greater than 4.5, the table by Koba et al. (1990) yields a lower

maximum wind than the table by Dvorak (1975) does, even after conversion to the same averaging time period (Nakazawa & Hoshino, 2009). *Faxai*'s peak maximum 1-min wind of 115 knots ($\approx 59 \text{ m}\cdot\text{s}^{-1}$) reported by the JTWC and the peak maximum 10-min wind of 85 knots ($\approx 44 \text{ m}\cdot\text{s}^{-1}$) reported by the JMA correspond to CI-numbers of 6.0 and 5.5 respectively. A CI-number discrepancy of 0.5 is not uncommon, given that some degree of subjectivity is unavoidable for the TC intensity estimation using the Dvorak technique.

After the violent dynamical adjustment of the initial vortex, the simulated *Faxais* in YSU-W, YSU-J, and MYNN-J intensified to about 955 hPa at 0900 UTC on September 8 and maintained their central pressures until 1500 UTC, when the northwestern part of the eyewall is over the Izu Peninsula. During this period, the central pressure with YSU-J is up to about 3 hPa lower than with MYNN-J. The maximum winds for YSU-W and YSU-J show large fluctuations and are up to about $5 \text{ m}\cdot\text{s}^{-1}$ stronger than those for MYNN-J. At 1700 UTC, the entire eyewall of *Faxai* began to experience strong friction over land and weakened dramatically. The simulated *Faxai* in YSU-J weakened a little faster than in MYNN-J in both the central pressure and maximum winds after 1700 UTC. In contrast, the simulated *Faxai* in MYJ-J intensified only slightly after the initial dynamical adjustment of the vortex

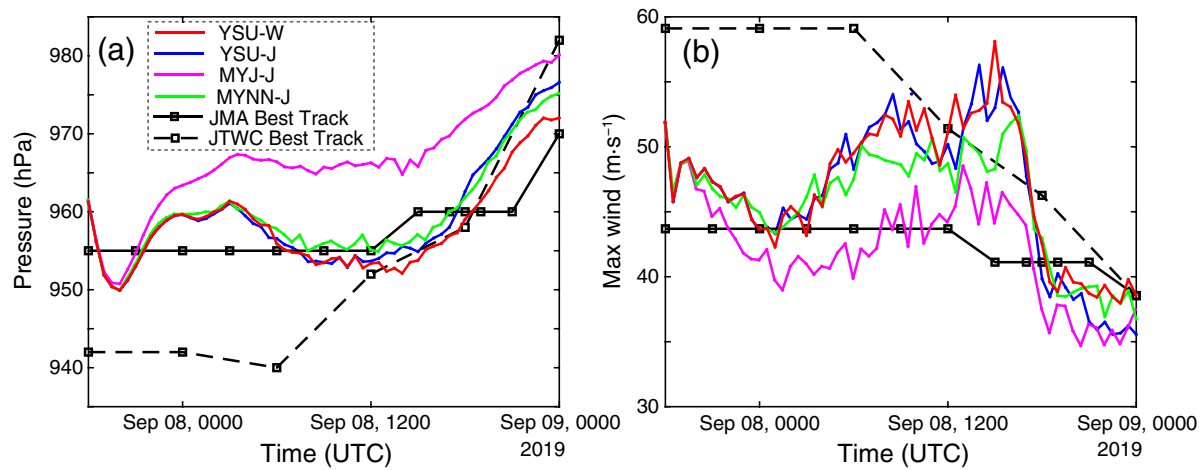


FIGURE 3 The time evolution of the (a) simulated sea-level pressure at the tropical cyclone center and (b) maximum 10 m horizontal winds are plotted against the best-track values issued by the Japan Meteorological Agency (JMA) and Joint Typhoon Warning Center (JTWC). The red, blue, magenta, and green solid lines represent YSU-W, YSU-J, MYJ-J, and MYNN-J respectively. The best-track values issued by the JMA and JTWC are plotted as black squares connected by black solid lines and black dashed lines respectively. YSU-W: Yonsei University PBL parametrization using WRF's default roughness length; YSU/MYJ/MYNN-J: Yonsei University/Mellor–Yamada–Janjić/Mellor–Yamada–Nakanishi–Niino PBL parametrization using the Japan Meteorological Agency's non-hydrostatic model roughness length. [Colour figure can be viewed at wileyonlinelibrary.com]

and kept its central pressure at around 966 hPa until 1500 UTC on September 8. During this period, the maximum surface winds in MYJ-J are weaker than in YSU-J and MYNN-J by 5–10 $\text{m}\cdot\text{s}^{-1}$. After 1500 UTC, the intensity of *Faxai* in MYJ-J as seen in both the central pressure and the maximum surface winds continued to weaken, though at a slower rate than YSU-J and MYNN-J. The maximum winds for MYJ-J after 1900 UTC are weaker than YSU-J and MYNN-J by only about 3 $\text{m}\cdot\text{s}^{-1}$ due to the slower decay of the intensity in MYJ-J. We note that this tendency of the MYJ PBL parametrization to make the TC weaker than YSU parametrization aligns with the recent studies of the WRF simulations of hurricanes *Wilma* (2005) and *Irma* (2017) (Nolan et al., 2021a, 2021b; Hendricks et al., 2021). Overall, the simulated intensities of *Faxai* in YSU-W, YSU-J, and MYNN-J are in good agreement with the best tracks, especially before and during the landfall, whereas *Faxai* in MYJ-J was weaker than observed, especially at landfall. From this point forward, detailed analysis results will be described for YSU-W, YSU-J, and MYNN-J.

3.2 | Vortex structure

3.2.1 | Reflectivity and horizontal winds at 2 km height

Typhoon *Faxai* made landfall with a compact and axisymmetric inner core. It underwent a series of

structural changes during the landfall, which were presented in detail in Part I (section 3). Figure 4 compares the observed composite C-band radar reflectivity with the simulated radar reflectivity at 10 cm wavelength during landfall for YSU-W, YSU-J, and MYNN-J. We note that the difference in refraction factor at 10 cm and C-band wavelengths are practically negligible for qualitative comparison. Throughout the period shown, the simulated radar reflectivity is stronger than that observed. We chose to use the Thompson microphysics scheme (Thompson et al., 2008) after confirming that it diminishes the positive bias of the radar reflectivity during landfall compared with the WRF Double Moment 6-class scheme (Lim & Hong, 2010).

At 1805 UTC on September 8, the reflectivity field for all simulations captures the basic structure of *Faxai*'s inner core, consisting of the high-reflectivity bands to the north and southeast of the eye, and the inner rain band in the northeast quadrant of the TC. *Faxai*'s eye as seen in the radar reflectivity field in YSU-J is smaller than in YSU-W and MYNN-J, and it is in better agreement with the observation. At landfall, the eye collapses, as seen in the composite radar reflectivity at 2005 UTC (Figure 4i). YSU-J and MYNN-J capture the observed collapse of the eye, whereas YSU-W maintains the eye (defined here as the low radar-reflectivity region near the TC center) throughout the simulation period. YSU-W failed to simulate the robust eyewall structure to the southeast of the eye (E2) during landfall, whereas YSU-J and MYNN-J partially capture

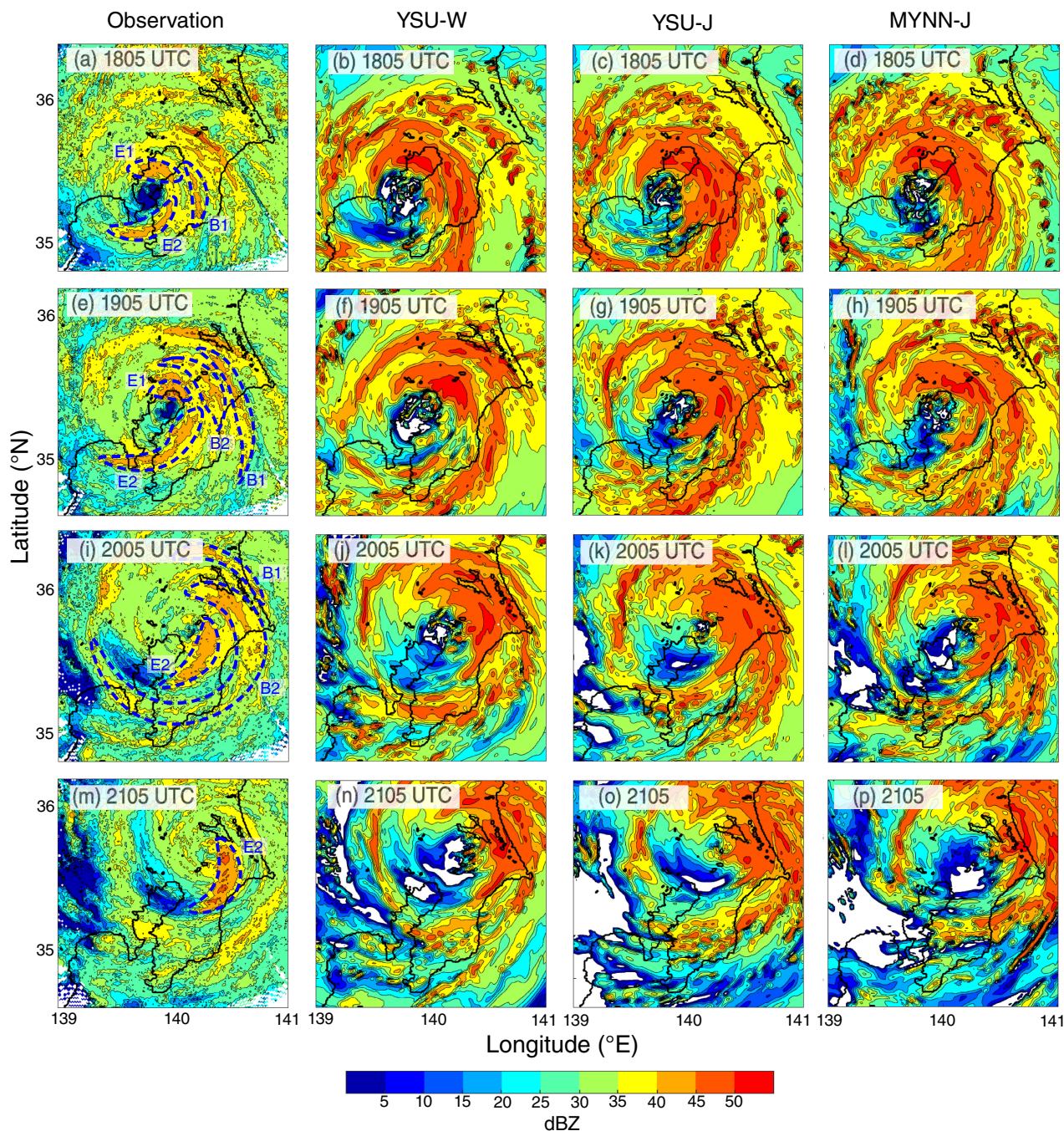


FIGURE 4 (a, e, i, m) Composite radar reflectivity at 2 km height over the Kanto region based on three ground-based C-band radars. The bands of strong reflectivity associated with the eyewall (E1, E2) and the rain bands (B1, B2) are indicated by blue dashed lines. The times are (a) 1805 UTC, (e) 1905 UTC, (i) 2005 UTC, and (m) 2105 UTC, on September 8. The corresponding 10 cm wavelength radar reflectivities at 2 km height are given for (b, f, j, n) Yonsei University (YSU)-W, (c, g, k, o) YSU-J, and (d, h, l, p) Mellor–Yamada–Nakanishi–Niino (MYNN)-J (W: WRF default roughness length; J: Japan Meteorological Agency’s non-hydrostatic model roughness length). [Colour figure can be viewed at [wileyonlinelibrary.com](https://onlinelibrary.wiley.com/doi/10.1002/qj.4663)]

the strong reflectivity band located to the southeast of the eye. The observed inner rain bands (B1 and B2) show a counterclockwise rotation, moving further away from the eye while increasing their axisymmetry. Across the simulations, the inner core, as seen in the radar reflectivity fields, loses its axisymmetry more rapidly than observed.

The simulated inner rain bands are more axisymmetric than observed throughout the period shown.

Figure 5 compares the observed and simulated horizontal winds at 2 km height. At 1805 UTC on September 8, all simulations capture two distinct peaks associated with the eyewall southeast of the eye and the inner rain band.

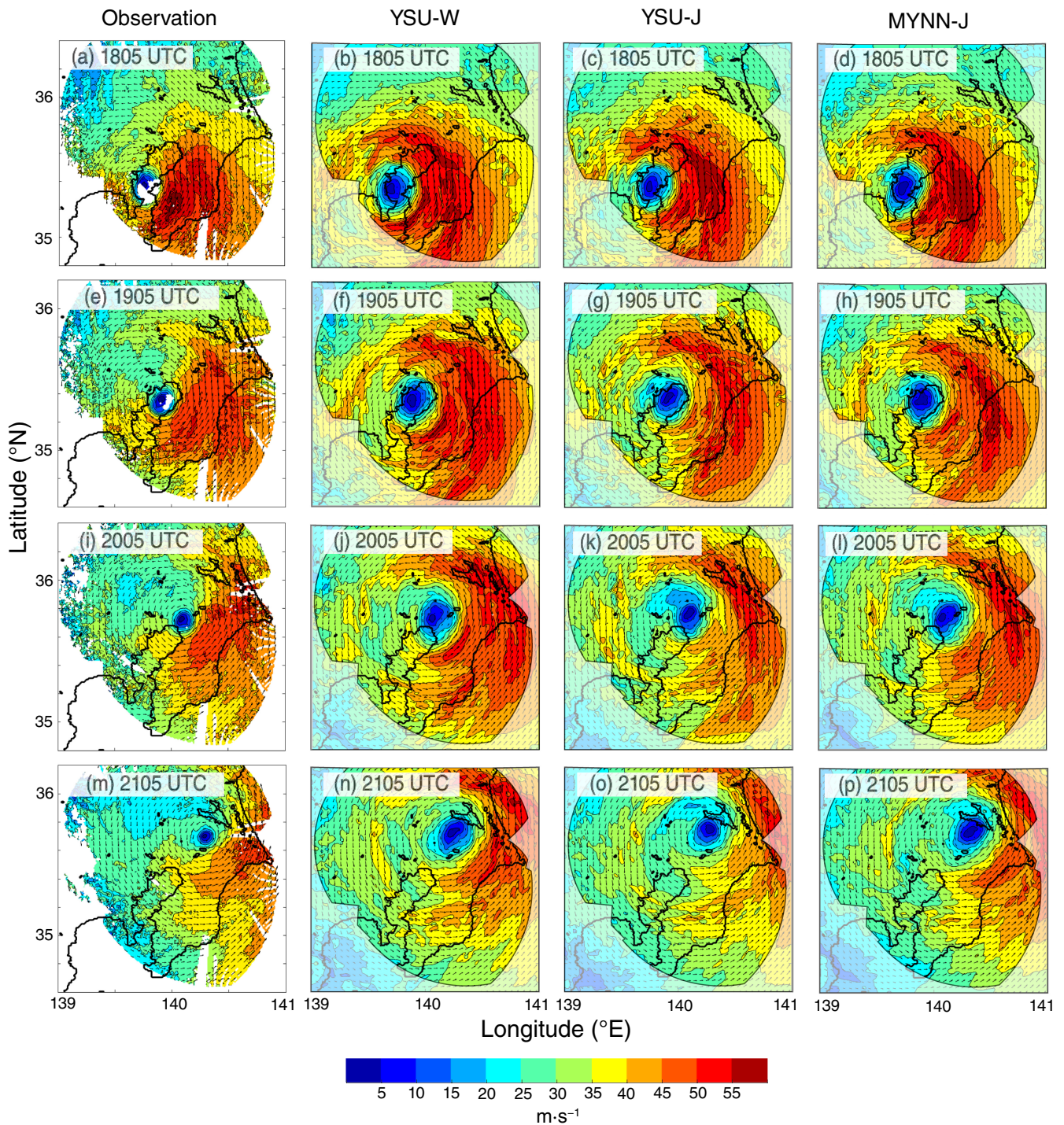


FIGURE 5 Same as Figure 4, but for horizontal winds at 2 km. The observational wind fields are based on the dual-Doppler analysis. In the simulation plots, areas outside the dual-Doppler analysis coverage are masked with a semi-transparent overlay. [Colour figure can be viewed at wileyonlinelibrary.com]

However, the simulated southeastern eyewall is not as clear as in the observation (E2), and the associated simulated peak winds are weaker than in the observation in YSU-J and MYNN-J. The simulated peak winds associated with the inner rain band, on the other hand, are stronger than the observation.

The two wind peaks associated with the eyewall and inner rain band are distinct for all simulations throughout the period shown. The wind peak associated with the eyewall in YSU-J decays faster than in the observation, whereas the one in MYNN-J is more robust, consistent with the observation. On the other hand, the inner-core

wind field of Faxai in YSU-J is more compact than in YSU-W and MYNN-J as also seen in the radar reflectivity, being more consistent with the observations. The outer wind peaks in all simulations are more axisymmetric than observed, corresponding to the simulated rain band being excessively axisymmetric (Figure 4). Based on the dual-Doppler analysis (Figure 5a,e), the area with horizontal wind speed less than $25 \text{ m}\cdot\text{s}^{-1}$ exists only very close to the center of Faxai throughout the period, indicating that the compact inner core was maintained during the landfall. The corresponding area in the simulations with horizontal winds less than $25 \text{ m}\cdot\text{s}^{-1}$ is much larger.

Figure 6 shows the map of the maximum winds (the wind swath) at 2 km height (Figure 6a–d) and the map of the time of the maximum winds at 2 km height (Figure 6e–h) for both the observation and the simulations. On the right side of the track, the maximum winds at 2 km in all simulations shown are up to $5 \text{ m}\cdot\text{s}^{-1}$ stronger than the observation. This is mainly because the simulated wind peaks associated with the inner rain band are stronger than the observations. The discrepancy with the observed maximum 2 km winds decreases with distance into the land in YSU-J, mainly due to the faster decay of the strong winds associated with the inner rain band. On the left side of

the track, the simulated maximum 2 km winds are greater than the observation by up to $10 \text{ m}\cdot\text{s}^{-1}$ near the track in the early stage of the landfall. This is mainly because the simulated 2 km winds on the left side of the track are stronger than the observations due to the overly axisymmetric rain band in the simulations.

3.2.2 | Axisymmetric tangential winds (\bar{V}_t)

Figure 7 compares the observed and simulated \bar{V}_t above the PBL during the landfall. The black star marks in Figure 7 indicate the location of the \bar{V}_t peak in the radius–altitude plane. At 1805 UTC, the observed upright structure with $\bar{V}_t > 40 \text{ m}\cdot\text{s}^{-1}$ associated with the eyewall is reproduced in all simulations. The peak \bar{V}_t associated with the eyewall in YSU-J decreases with time, from about $42 \text{ m}\cdot\text{s}^{-1}$ at 1805 UTC to $35 \text{ m}\cdot\text{s}^{-1}$ at 2105 UTC, which is in quantitative agreement with the observation, whereas the corresponding peak \bar{V}_t in YSU-W and MYNN-J is stronger throughout the period shown. The simulated peaks of \bar{V}_t are radially approximately 5 km further from the TC center compared with the observations. Also, the observed oscillation in the maximum \bar{V}_t and RMW with height,

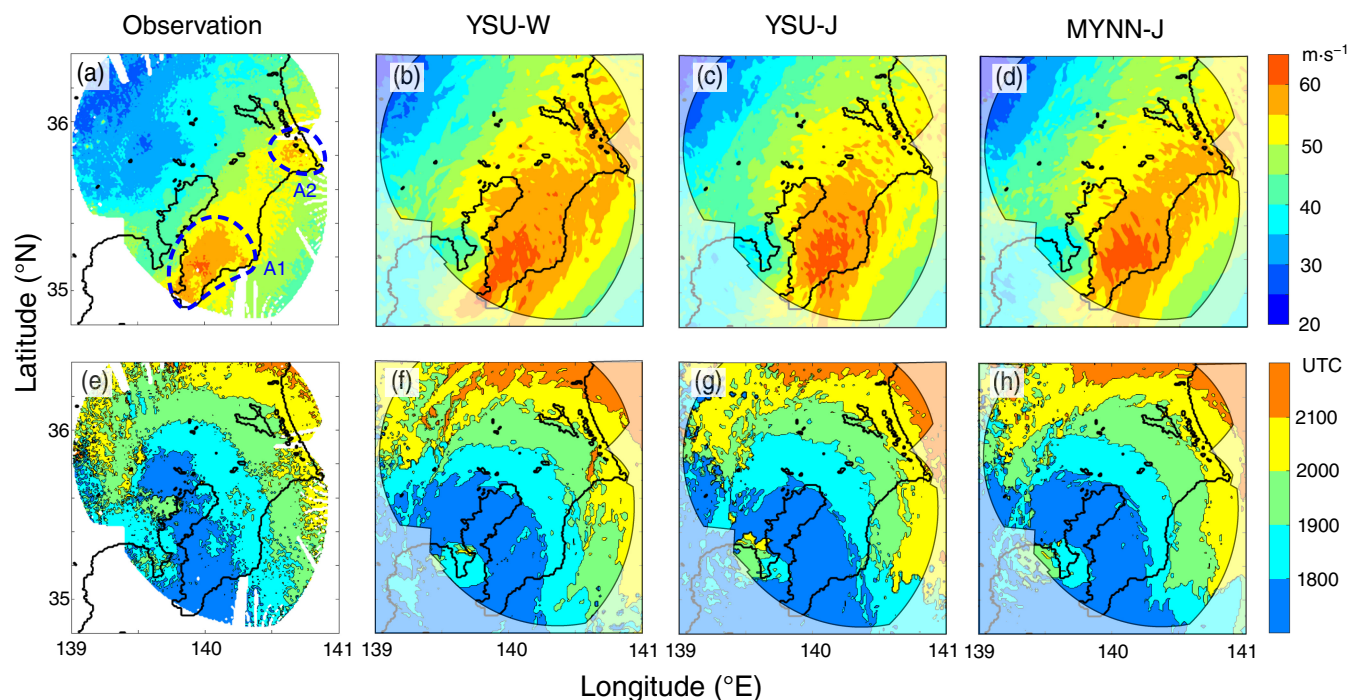


FIGURE 6 (a–d) Map of the maximum winds at 2 km height between 1700 UTC and 2300 UTC on September 8. (e–h) Time when the 2 km winds peaked. (a, e) Observational plots based on the dual-Doppler analysis. The two distinct areas with maximum 2 km winds stronger than $55 \text{ m}\cdot\text{s}^{-1}$ are encircled by blue dashed lines (A1 and A2, respectively) in (a); (b, f) for Yonsei University (YSU)-W, (c, g) for YSU-J, and (d, h) for Mellor–Yamada–Nakanishi–Niino (MYNN)-J (W: WRF default roughness length; J: Japan Meteorological Agency’s non-hydrostatic model roughness length). In the simulation plots, the area outside the coverage of the dual-Doppler analysis is covered by the half-transparent mask. The units for the color bars are $\text{m}\cdot\text{s}^{-1}$ and UTC on September 8. [Colour figure can be viewed at wileyonlinelibrary.com]

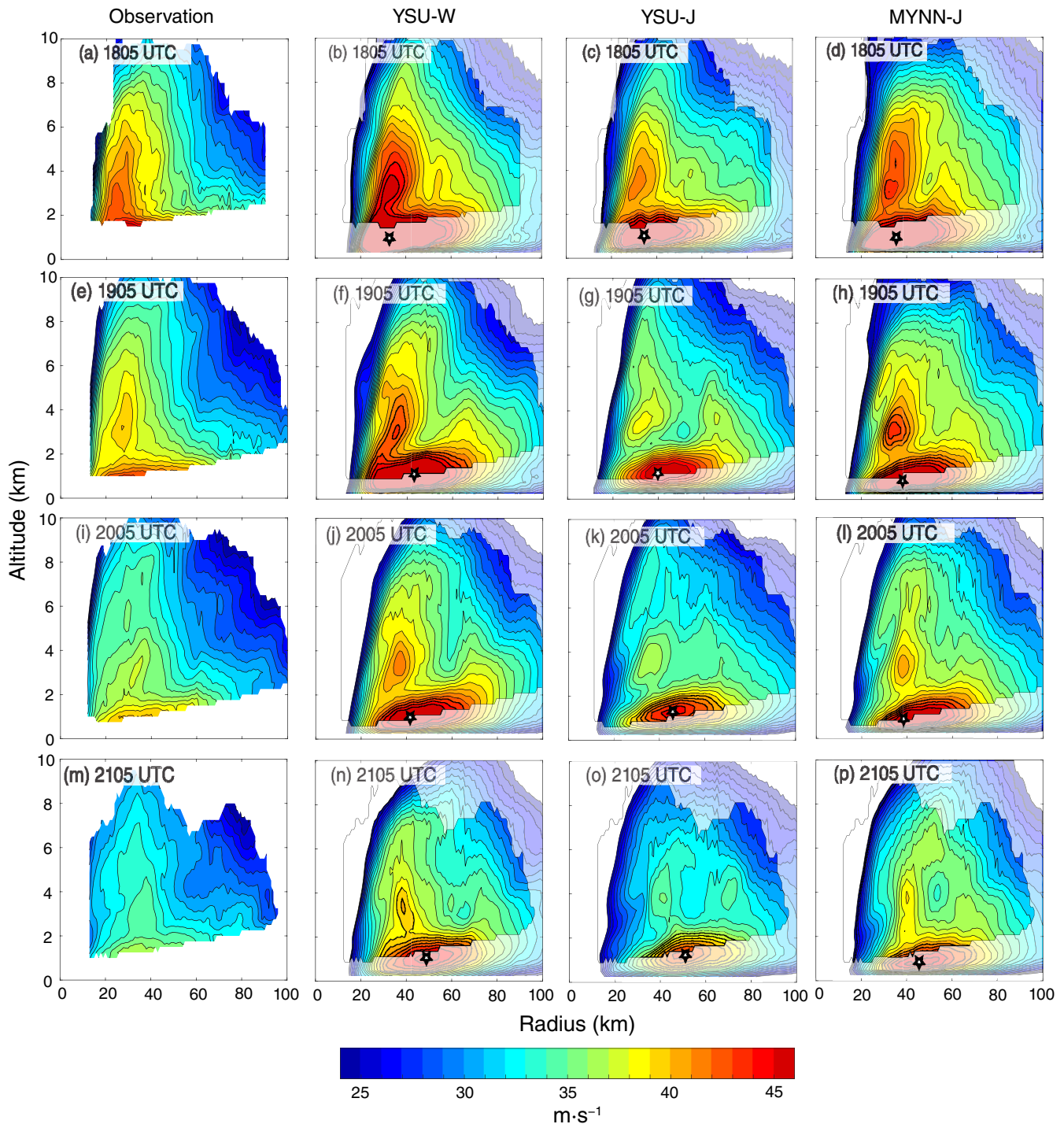


FIGURE 7 (a, e, i, m) The axisymmetric tangential wind field \bar{V}_t above the PBL up to 10 km, based on the dual-Doppler analysis. The times shown are the same as in Figures 4 and 5. The coverage in the r - z plane with valid \bar{V}_t changes with time due to the change in the position of *Faxai* relative to the three radars. The other columns are same as the first column but for (b, f, j, n) Yonsei University (YSU)-W, (c, g, k, o) YSU-J, and (d, h, l, p) Mellor–Yamada–Nakanishi–Niino (MYNN)-J (W: WRF default roughness length; J: Japan Meteorological Agency’s non-hydrostatic model roughness length). In the simulation plots, the area outside the valid \bar{V}_t based on the dual-Doppler analysis is covered by the half-transparent mask. The locations of the simulated PBL jets are indicated by black star marks. [Colour figure can be viewed at wileyonlinelibrary.com]

together with multiple peaks in \bar{V}_t in the vertical direction after 1905 UTC, is reproduced in all simulations. After 1905 UTC, another peak of simulated \bar{V}_t associated with

the inner rain band is clearly seen between $r = 60$ km and $r = 80$ km. Such a secondary peak is observed at 2005 UTC (Figure 7i) around $r = 60$ km associated with the inner

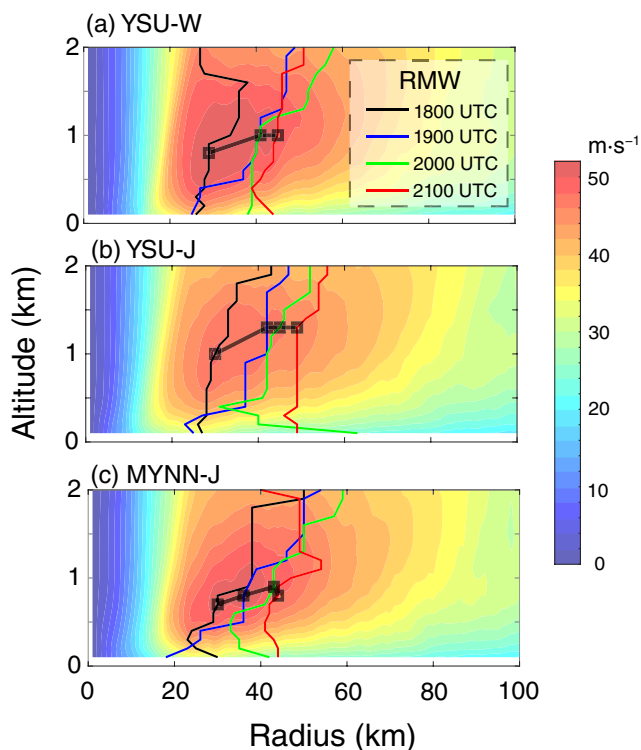


FIGURE 8 The axisymmetric tangential wind field \bar{V}_t in the planetary boundary layer at 1800 UTC (color shadings), together with the hourly locations of the radius of maximum wind (RMW), for (a) Yonsei University (YSU)-W, (b) YSU-J, and (c) Mellor–Yamada–Nakanishi–Niino (MYNN)-J (W: WRF default roughness length; J: Japan Meteorological Agency's non-hydrostatic model roughness length). The hourly locations of the peak \bar{V}_t in the radius–altitude plane are indicated by black squares connected by black solid lines. [Colour figure can be viewed at wileyonlinelibrary.com]

rain band B2, but is not as clear or robust as in the simulations. The pronounced secondary peak in the simulations is likely due to an excessively axisymmetric inner rain band.

The \bar{V}_t in the PBL at 1800 UTC along with the hourly location of the RMW for YSU-W, YSU-J, and MYNN-J are compared in Figure 8. The locations of the simulated \bar{V}_t peaks in the radius–altitude plane are indicated by the black squares. The peak \bar{V}_t in MYNN-J is located at the lowest altitude. The peak \bar{V}_t in YSU-J is located higher than in YSU-W. The RMW in the PBL is tilted more horizontally in MYNN-J than in both YSU-W and YSU-J, and the outward migration of the \bar{V}_t with time is evident in all simulations. Additionally, the height of the simulated \bar{V}_t peak generally increases with time.

The observed and simulated radial profiles of \bar{V}_t at 2 km ($\bar{V}_{t,2km}$) at 1800 UTC and 2000 UTC are compared in Figure 9. From 1800 UTC to 2000 UTC, the observed inner

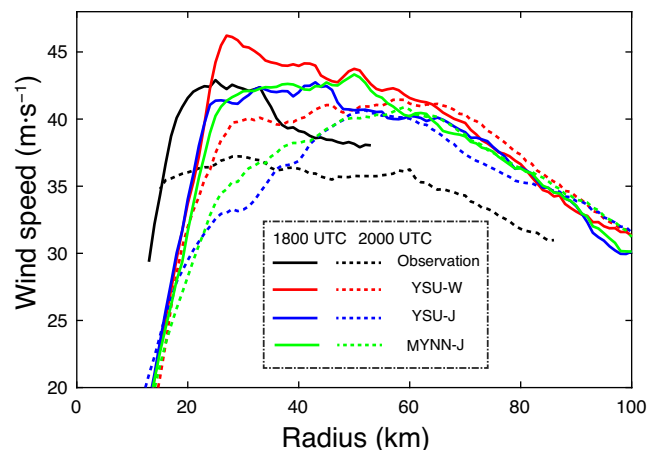


FIGURE 9 The radial distribution of \bar{V}_t at 2 km ($\bar{V}_{t,2km}$) at 1800 UTC (solid lines) and 2000 UTC (dashed lines) on September 8. The black lines are observational plots based on the dual-Doppler analysis, whereas the red, blue, and green lines are the results from Yonsei University (YSU)-W, YSU-J, and Mellor–Yamada–Nakanishi–Niino (MYNN)-J respectively (W: WRF default roughness length; J: Japan Meteorological Agency's non-hydrostatic model roughness length). [Colour figure can be viewed at wileyonlinelibrary.com]

core winds within $r = 40$ km decayed rapidly, resulting in a flat radial profile of \bar{V}_t at 2000 UTC. The observed $\bar{V}_{t,2km}$ radially inside the secondary peak continues to decrease with time, whereas $\bar{V}_{t,2km}$ outside of the secondary peak remains almost unchanged. Similarly, the inner core $\bar{V}_{t,2km}$ in YSU-W decays rapidly from 1800 UTC to 2000 UTC, resulting in an almost flat radial profile within the inner rain band at 2000 UTC, and it continues to decrease with time. The $\bar{V}_{t,2km}$ in YSU-J is closer to the observation than in YSU-W outside the observed RMW. However, the inner core $\bar{V}_{t,2km}$ in YSU-J decays faster than the observation, resulting in a single peak $\bar{V}_{t,2km}$ profile from 1900 UTC, which is not the case in the observed radial profile of $\bar{V}_{t,2km}$. The peak of $\bar{V}_{t,2km}$ in YSU-J is located slightly inside the inner rain band and propagates radially outward from about 40 km to 60 km. In MYNN-J, the $\bar{V}_{t,2km}$ associated with the eyewall decayed more slowly than in YSU-J, resulting in a flatter $\bar{V}_{t,2km}$ profile compared with YSU-J.

Figure 10a compares the time evolution of the maximum $\bar{V}_{t,2km}$ ($\bar{V}_{t,2km,max}$) between the observations and the simulations. $\bar{V}_{t,2km,max}$ in YSU-W is $4 \text{ m}\cdot\text{s}^{-1}$ stronger than the observation at 1800 UTC, but the discrepancy grows to $7 \text{ m}\cdot\text{s}^{-1}$ at 2200 UTC, due to the slower decay of $\bar{V}_{t,2km,max}$ in YSU-W. On the other hand, $\bar{V}_{t,2km,max}$ in YSU-J and MYNN-J agrees well with the 1800 UTC observation at $43 \text{ m}\cdot\text{s}^{-1}$. Observed $\bar{V}_{t,2km,max}$ decreases to about $34 \text{ m}\cdot\text{s}^{-1}$ at 2200 UTC, whereas $\bar{V}_{t,2km,max}$ in YSU-J and MYNN-J

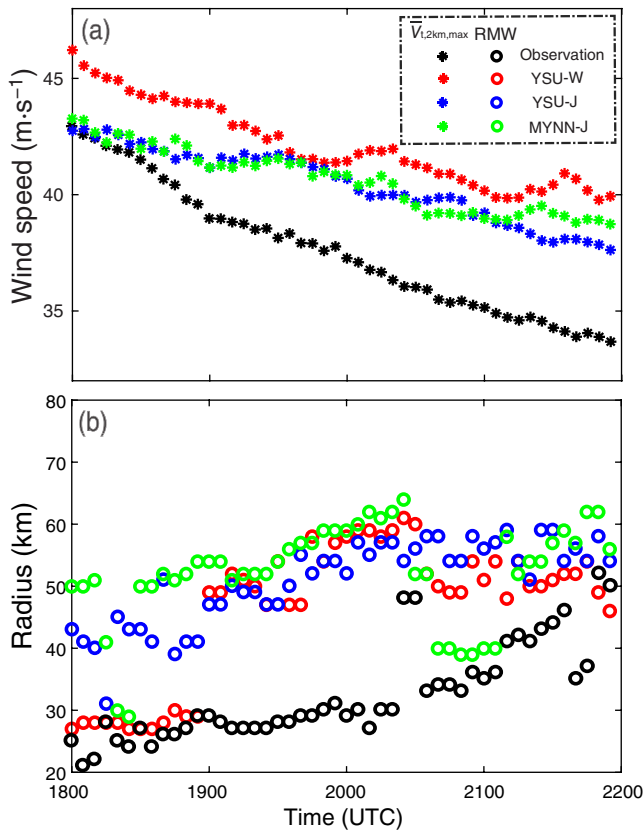


FIGURE 10 The time evolution of (a) the maximum $\bar{V}_{t,2km}$ ($\bar{V}_{t,2km,max}$) and (b) the radius of maximum wind (RMW) at 2 km. The black asterisks and circles in (a) and (b) are observational plots based on the dual-Doppler analysis, whereas the red, blue, and green marks represent Yonsei University (YSU)-W, YSU-J, and Mellor–Yamada–Nakanishi–Niino (MYNN)-J respectively (W: WRF default roughness length; J: Japan Meteorological Agency’s non-hydrostatic model roughness length). [Colour figure can be viewed at wileyonlinelibrary.com]

decreases only to about $37 \text{ m}\cdot\text{s}^{-1}$ and $38 \text{ m}\cdot\text{s}^{-1}$ respectively at 2200 UTC.

The time evolution of the RMW at 2 km in the observations and simulations is compared in Figure 10b. The observed RMW gradually increases from about 25 km at 1800 UTC to 30 km at 2000 UTC, and then rapidly increases to about 50 km at 2200 UTC. The RMW in YSU-W jumps from about 30 km, corresponding to the eyewall location, to about 50 km to 60 km at 1900 UTC, slightly inside the inner rain band, and remains almost unchanged until 2200 UTC. The RMW in YSU-J and MYNN-J increases from about 40 km at 1800 UTC to about 60 km at 2000 UTC and remains almost unchanged. Throughout the period shown, the RMW at 2 km in YSU-J and MYNN-J is located just inside the inner rain band. Consequently, the simulations significantly overestimate the RMW, which is associated with the eyewall in reality.

3.3 | Inner core PBL wind profiles over Narita Airport

Narita Airport is located to the right side of *Faxai*’s track and experienced the passage of the eyewall.

Figure 11a,e,i,m shows the time evolution of the observed wind reduction factor and the PBL wind profiles over Narita Airport. The black circles in Figure 11a show the observed wind reduction factor $F_{2km,obs} = v_s/v_{2km}$, where v_s and v_{2km} are surface winds and 2 km winds respectively. The blue circles in Figure 11a show the empirical model for the wind reduction factor $F_{2km,model} = f_{jet}F_s$, where the jet strength $f_{jet} = v_{jet}/v_{2km}$ is the ratio between the PBL jet wind speed (the maximum wind speed below 2 km) to the 2 km wind speed, and F_s is the wind reduction factor from the top of the logarithmic layer. Given the surface roughness length z_0 , the heights of the PBL jet (H_{jet}) and the anemometer ($H_a = 10 \text{ m}$), the expression for F_s is as follows:

$$F_s \approx \frac{\log(H_a/z_0)}{\log(\alpha H_{jet}/z_0)}, \quad (8)$$

where α is an arbitrary parameter and taken as 0.5 in the analysis presented here. The details of the empirical model are described in Part I. Figure 11e shows the time evolution of f_{jet} and F_s , to compare the contribution from each term. Figure 11i shows v_{jet} , v_s , and v_{2km} . Figure 11m shows the PBL wind profile based on the velocity–azimuth display analysis. The black squares indicate the height of the PBL jet at each time. The other columns in Figure 11 are the same as the first column but for the simulations YSU-W (Figure 11b,f,j,n), YSU-J (Figure 11c,g,k,o), and MYNN-J (Figure 11d,h,l,p). $F_{2km,WRF} = v_s/v_{2km}$ is the wind reduction factor calculated directly from v_s and v_{2km} in the WRF simulations, whereas $F_{2km,model}$ is calculated from the PBL jet and surface properties $f_{jet} = v_{jet}/v_{2km}$, H_{jet} , and z_0 in the simulations.

The PBL jets associated with the inner rain band (B2) and the eyewall (E2) are visible in Figure 11m. After the passage of the rain band B2, the observed v_{2km} decreases with the approach of the center of *Faxai* from 1900 UTC to 2100 UTC. Correspondingly, the simulated v_{2km} decreases from 1900 UTC to 2100 UTC. Across the simulations, the PBL jet associated with the eyewall above Narita Airport is located higher than observed. The simulated peak of v_{jet} associated with the inner rain band is stronger than the observations. The v_{jet} associated with the eyewall in YSU-W is slightly stronger than observed, whereas in YSU-J and MYNN-J it is slightly weaker than observed. The f_{jet} in YSU-W is smaller than observed and remains relatively constant over time, whereas in both YSU-J and MYNN-J it captures the observed distinct peak

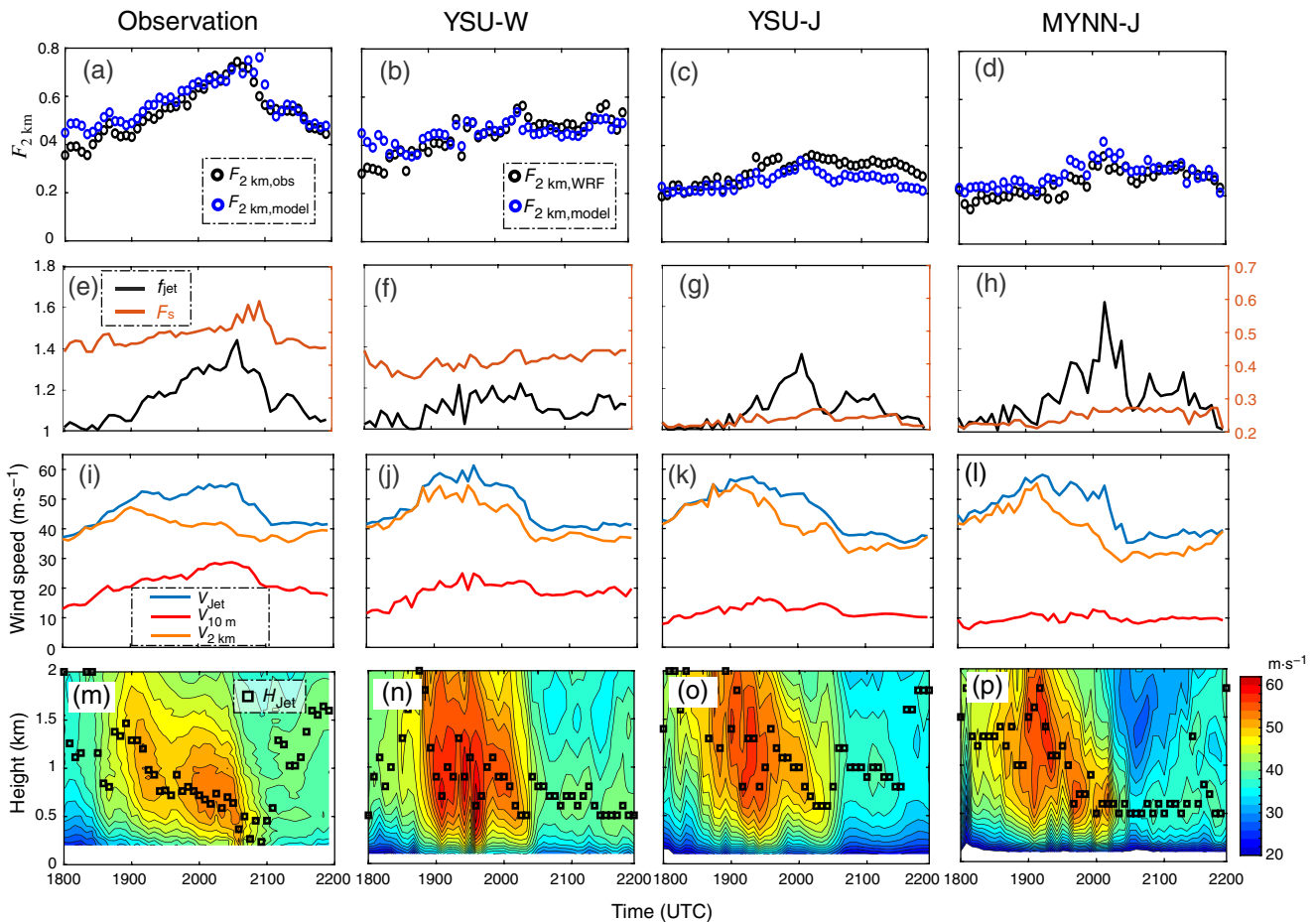


FIGURE 11 Observed and simulated wind profiles and the wind reduction factors at Narita Airport. (a) Observed wind reduction factor $F_{2\text{ km,obs}}$ (black circles) and the empirical model of the wind reduction factor $F_{2\text{ km,model}}$ (blue circles) based on radar velocity–azimuth display (VAD) analysis. (e) The jet strength f_{jet} (black line) and the wind reduction factor from the top of logarithmic layer F_s (orange line). (i) the wind speeds at 2 km ($v_{2\text{ km}}$, orange line), the PBL jet wind speed (v_{jet} , blue line), and the surface winds (v_s , red line) based on the radar VAD analysis and Automated Meteorological Data Acquisition System observation. (m) The profile of winds in the PBL over Narita Airport obtained from the VAD analysis. The height of the PBL jet defined as the wind maxima is shown in black squares in (m). The other columns are the same as the first column but for (b, f, j, n) Yonsei University (YSU)-W, (c, g, k, o) YSU-J, and (d, h, l, p) Mellor–Yamada–Nakanishi–Niino (MYNN)-J (W: WRF default roughness length; J: Japan Meteorological Agency’s non-hydrostatic model roughness length). [Colour figure can be viewed at wileyonlinelibrary.com]

during the eyewall passage. We note that the overestimation of the peak f_{jet} in MYNN-J may be related to the fact that the center of *Faxai* in MYNN-J comes closer to Narita Airport than both the best track and other simulations. All simulations overestimate H_{jet} associated with the eyewall. The overestimation is particularly significant in YSU-J and MYNN-J. As such, F_s in both YSU-J and MYNN-J is consistently smaller than observed. During the period shown, the empirical model for the simulated wind reduction factor $F_{2\text{ km,model}}$ captures all the peaks in $F_{2\text{ km,WRF}}$ over Narita Airport. This indicates that the surface roughness length z_0 and the PBL jet properties (f_{jet} and H_{jet}) are crucial for the accurate simulation of the inner core surface wind peaks v_s through the logarithmic law $F_{2\text{ km,model}}$.

The observed and simulated peak in v_s occurred inside the $v_{2\text{ km}}$ peak. The maximum v_s at Narita Airport in both YSU-W and YSU-J occurred around 1930 UTC, associated with the passage of the inner rain band, whereas the actual maximum v_s was observed at 2030 UTC under the eyewall PBL jet. The simulated peak v_s associated with the eyewall in both YSU-W and YSU-J is considerably weaker than the observation. The v_s in MYNN-J had a peak at around 2000 UTC associated with the eyewall, but its magnitude is substantially weaker than the observed peak v_s . The analysis presented here suggests that the accurate simulation of the observed low and strong PBL jet associated with the eyewall is crucial for the accurate simulation of the inner core v_s peaks. We note that the v_s observed at airports tends to be stronger due to the “open exposure” environment.

The reduced surface roughness at airport observing stations is due to man-made open spaces such as runways and staging areas, and these features are not usually captured in land-use datasets on the order of a few kilometers and with limited land-use categories. This effect is not corrected in the present analysis.

3.4 | Surface winds

We compare the simulated and observed 10 m winds ($v_{10\text{m}}$) and 2 km winds ($v_{2\text{km}}$) at 12 AMeDAS stations (P1 to P12) near the track of *Faxai* in Figures 12 and 13. The locations of the AMeDAS stations are shown in Figure 2b. The observed surface winds are adjusted to 10 m winds $v_{10\text{m}}$ based on the logarithmic wind profile and the estimated roughness length at each station. The details of the 10 m adjustment are described in Part I (appendix B). The observed $v_{2\text{km}}$ over each AMeDAS station is obtained from the dual-Doppler radar analysis. The thin black lines are the maximum and minimum 1-min winds every 10 min observed with the AMeDAS stations. The simulated 2 km winds and 10 m winds are shown as colored filled circles and colored solid lines (red: YSU-W; blue: YSU-J; green: MYNN-J) respectively. In Figures 12 and 13, the mean absolute error (MAE) and mean bias (MB) of $v_{10\text{m}}$ for YSU-W, YSU-J, and MYNN-J at each station are also shown. MAE and MB are defined as follows:

$$\begin{aligned} \text{MAE} &= \frac{\sum_i |v_{10\text{m,WRF}} - v_{10\text{m,obs}}|}{N_t}, \\ \text{MB} &= \frac{\sum_i (v_{10\text{m,WRF}} - v_{10\text{m,obs}})}{N_t}, \end{aligned} \quad (9)$$

where $v_{10\text{m,WRF}}$ and $v_{10\text{m,obs}}$ are the simulated 10 m winds and observed 10-min sustained winds adjusted to 10 m respectively. The summation \sum_i is taken over $N_t = 711$ data points recorded every minute from 1205 UTC to 2355 UTC on September 8.

The overall time evolution of the simulated 2 km winds is in good agreement with the observations at all the 12 AMeDAS stations, whereas the first peaks in simulated $v_{2\text{km}}$ are up to $10\text{ m}\cdot\text{s}^{-1}$ stronger than the observations at most of the stations. The later peaks in simulated $v_{2\text{km}}$ are in good agreement with observation. The first $v_{2\text{km}}$ peaks in YSU-J and YSU-W are almost the same in magnitude, whereas the later peaks are about $5\text{ m}\cdot\text{s}^{-1}$ weaker in YSU-J than in YSU-W. The dips of simulated $v_{2\text{km}}$ are generally deeper and wider than in the observation, resulting in considerably weaker simulated $v_{2\text{km}}$ within the observed RMW compared with the observation. The observed and simulated peaks in $v_{2\text{km}}$ occur about 2 hr before the minimum of $v_{2\text{km}}$. We note that these $v_{2\text{km}}$ peaks before the dips

are associated with the passage of the inner rain band. The observed $v_{2\text{km}}$ peaks likely associated with the eyewall are visible at some stations (e.g., P1 to P5, P8, P10), but are not visible in the simulations.

The difference in $v_{10\text{m}}$ between YSU-W and YSU-J are considerable at all AMeDAS stations shown. At all AMeDAS stations except Ryugasaki (P9), $v_{10\text{m}}$ in YSU-W are stronger than observed throughout the period shown, indicating that the surface roughness lengths for YSU-W are too small. The significant overestimation of $v_{10\text{m}}$ in YSU-W is also evident from the positive MB ranging from 3 to $7\text{ m}\cdot\text{s}^{-1}$. By modifying the surface roughness length, $v_{10\text{m}}$ in YSU-J is in much better agreement with the observation at most of the stations. The improvement is also seen as the decrease in MAE for both YSU-J and MYNN-J. However, at many stations (such as at P2, P5, P6, P7, P8, P11, and P12), the simulated peaks of $v_{10\text{m}}$ occur about 0.5 to 1 hr earlier than the actual observed peaks. The simulation thus misses the observed $v_{10\text{m}}$ peak that occurs well inside the RMW at 2 km during the passage of the eyewall. For example, at Chiba (P5), $v_{10\text{m}}$ in both YSU-J and MYNN-J agrees very well with the observed $v_{10\text{m}}$ until it peaks at around 1830 UTC, but misses the actual observed wind maximum at 1924 UTC. The observed peak of 10 m adjusted winds $v_{10\text{m}}$ is about $22\text{ m}\cdot\text{s}^{-1}$, whereas the simulated peak $v_{10\text{m}}$ was about $15\text{ m}\cdot\text{s}^{-1}$. We note that such a discrepancy may be due to the simulated PBL jet associated with the eyewall being weaker and higher than observed, as in the case of the simulated PBL winds over Narita Airport discussed in Section 3.3.

At P7–P12, located further inland, the simulated $v_{2\text{km}}$ inside the RMW is stronger in YSU-J than in MYNN-J. Correspondingly, the $v_{10\text{m}}$ in YSU-J are stronger than in MYNN-J at these stations. This is probably due to the fact that the simulated inner core of *Faxai* in YSU-J was more compact than in MYNN-J, and that the $\bar{V}_{1,2\text{km}}$ near the center in YSU-J are stronger than in MYNN-J. In particular at Kashima (P11), the simulated $v_{2\text{km}}$ in YSU-J is in almost perfect agreement with the observation. The outer core $v_{10\text{m}}$ in YSU-J is also in almost perfect agreement with the observation. However, the inner core $v_{10\text{m}}$ in YSU-J is consistently weaker than observed. This means that the WRF simulations significantly underestimate $F_{2\text{km}}$ at Kashima (P11) during the passage of the eyewall. Similar underestimation of inner core winds is seen at other AMeDAS stations, such as at Kisarazu (P2), Chiba (P5), and Sakura (P7), which are all located on the right side of the track of *Faxai*. Such underestimations of inner core $F_{2\text{km}}$ in the simulations are probably due to the weaker and/or higher eyewall PBL jet in the simulations compared with the observation, as illustrated in detail in the PBL winds over Narita Airport in Section 3.3.

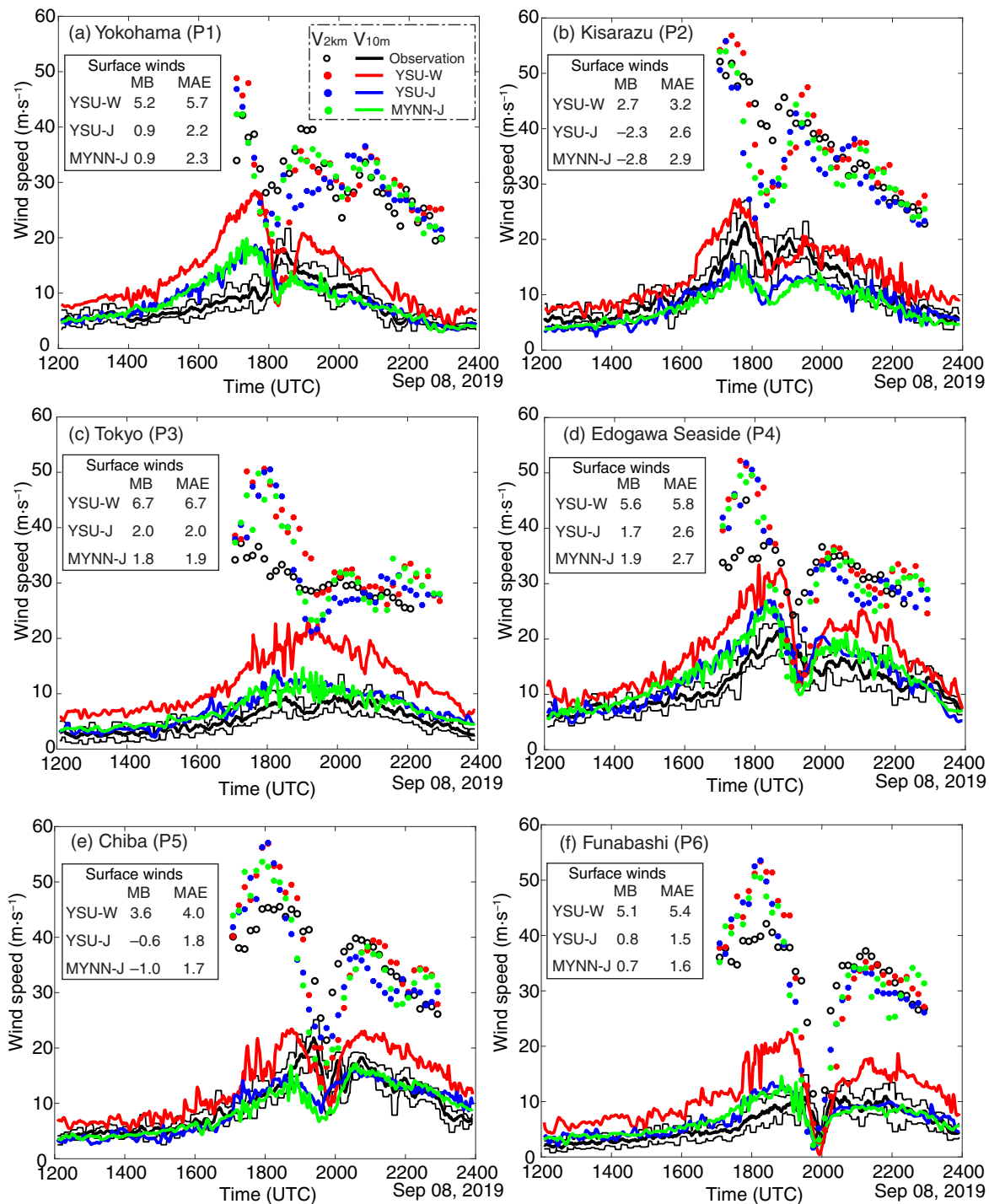


FIGURE 12 The comparison of observed and simulated surface winds and 2 km winds at stations directly affected by the passage of the inner core of Typhoon *Faxai*. The black circles show the 2 km wind speed obtained by the dual-Doppler analysis. The red, blue, and green asterisks show the 2 km wind speed for Yonsei University (YSU)-W, YSU-J, and Mellor–Yamada–Nakanishi–Niino (MYNN)-J respectively (W: WRF default roughness length; J: Japan Meteorological Agency’s non-hydrostatic model roughness length). The thick black lines are observed surface 10-min wind, whereas the thin black lines are maximum and minimum 1-min wind every 10 min. The red, blue, and green lines are the surface (10 m) winds for YSU-W, YSU-J, and MYNN-J respectively. Note that the observed surface winds are adjusted to 10 m height based on the logarithmic wind profile and estimated surface roughness length at each station. The stations shown are (a) Yokohama (P1), (b) Kisarazu (P2), (c) Tokyo (P3), (d) Edogawa Seaside (P4), (e) Chiba (P5), and (f) Funabashi (P6). MB: mean bias; MAE: mean absolute error. [Colour figure can be viewed at wileyonlinelibrary.com]

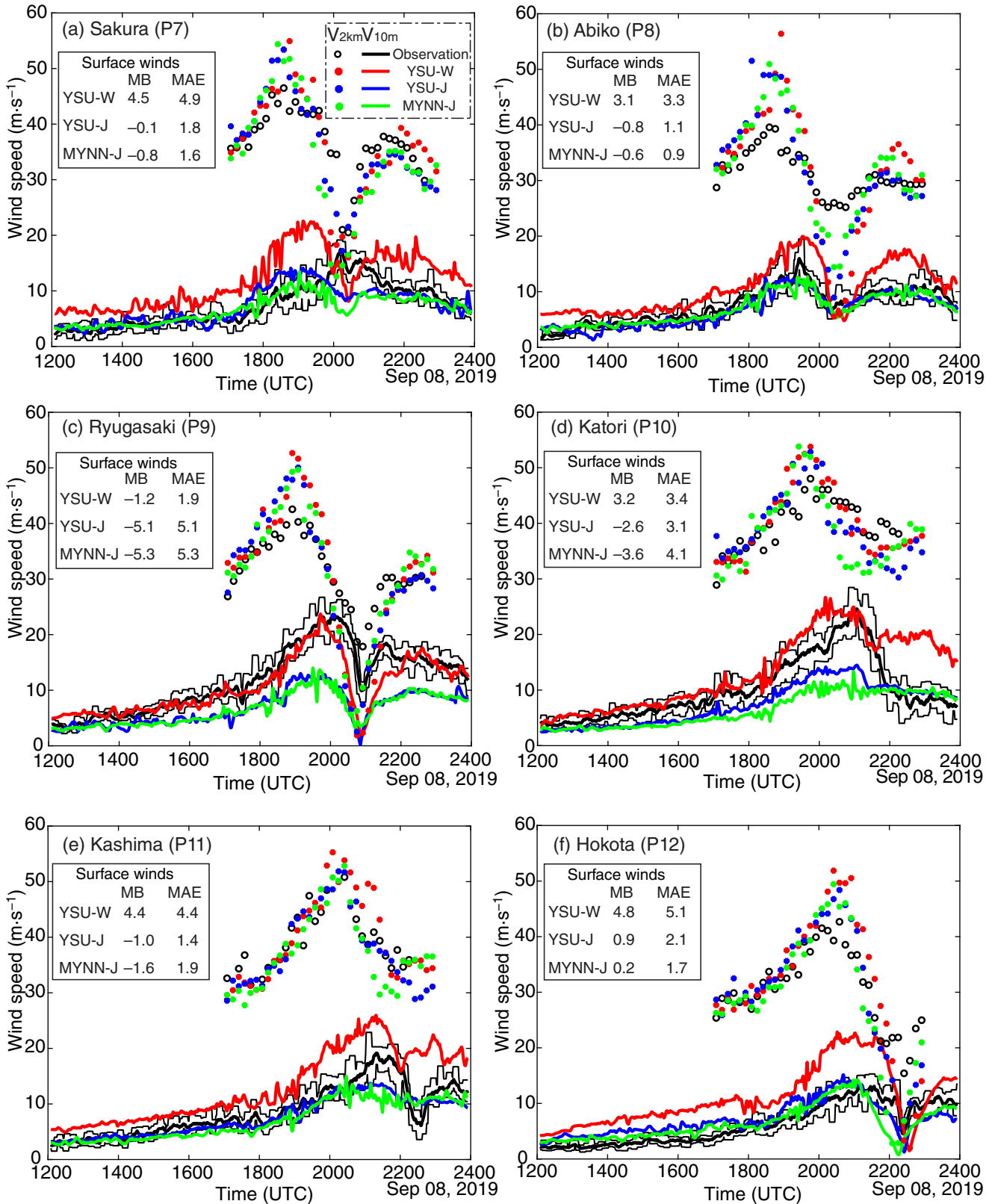


FIGURE 13 Same as Figure 12, but for (a) Sakura (P7), (b) Abiko (P8), (c) Ryugasaki (P9), (d) Katori (P10), (e) Kashima (P11), and (f) Hokota (P12). [Colour figure can be viewed at wileyonlinelibrary.com]

TABLE 4 Mean absolute error (MAE, $\text{m}\cdot\text{s}^{-1}$) and mean bias (MB, $\text{m}\cdot\text{s}^{-1}$) of the simulated surface winds.

AMeDAS station	Statistic	Simulation		
		YSU-W	YSU-J	MYNN-J
P1 Yokohama	MB	5.2	0.9	0.9
	MAE	5.7	2.2	2.3
P2 Kisarazu	MB	2.7	-2.3	-2.8
	MAE	3.2	2.6	2.9
P3 Tokyo	MB	6.7	2.0	1.8
	MAE	6.7	2.0	1.9
P4 Edogawa Seaside	MB	5.6	1.7	1.9
	MAE	5.8	2.6	2.7
P5 Chiba	MB	3.6	-0.6	-1.0
	MAE	4.0	1.8	1.7
P6 Funabashi	MB	5.1	0.8	0.7
	MAE	5.4	1.5	1.6
P7 Sakura	MB	4.5	-0.1	-0.8
	MAE	4.9	1.8	1.6
P8 Abiko	MB	3.1	-0.8	-0.6
	MAE	3.3	1.1	0.9
P9 Ryugasaki	MB	-1.2	-5.2	-5.3
	MAE	1.9	5.1	5.3
P10 Katori	MB	3.2	-2.6	-3.6
	MAE	3.4	3.1	4.1
P11 Kashima	MB	4.4	-1.0	-1.6
	MAE	4.4	1.4	1.9
P12 Hokota	MB	4.8	0.9	0.2
	MAE	5.1	2.1	1.7

Abbreviation: AMeDAS, Automated Meteorological Data Acquisition System.

Table 4 summarizes the MB and MAE of $v_{10\text{m}}$ for YSU-W, YSU-J, and MYNN-J for the period shown in Figures 12 and 13. The substantial positive bias of $v_{10\text{m}}$ in YSU-W is mitigated in both YSU-J and MYNN-J, except at Ryugasaki (P9) and Katori (P10), where z_0 is likely overestimated in YSU-J and MYNN-J. At stations located on the right side of *Faxai*'s track, such as Kisarazu (P2), Chiba (P5), Sakura (P7), Katori (P10), and Kashima (P11), MYNN-J exhibits a larger negative bias in $v_{10\text{m}}$ compared with YSU-J.

Figure 14 shows the maps of the observed and simulated maximum 10-min sustained winds (the wind swath) at 10 m height. The observational wind swath is constructed by spatially interpolating anemometer data, followed by the 10 m adjustment using the estimated z_0 map based on the land-use types. The details of the observed wind swath analysis are presented in Part I (appendix B).

Clearly, the maximum $v_{10\text{m}}$ in YSU-W is stronger than the observation almost everywhere in the Kanto region. To the right of the track of *Faxai*, the maximum $v_{10\text{m}}$ in YSU-W is about $4\text{ m}\cdot\text{s}^{-1}$ stronger in large areas, whereas on the left of the track the maximum $v_{10\text{m}}$ in YSU-W is up to $10\text{ m}\cdot\text{s}^{-1}$ stronger than in the observation. We note that the simulated maximum 2 km winds $v_{2\text{km}}$ on the right side of the track is about $5\text{ m}\cdot\text{s}^{-1}$ stronger than observed, whereas that on the left side of the track is about $10\text{ m}\cdot\text{s}^{-1}$ stronger than observed near the track, as described in Section 3.2 (Figure 6). In YSU-J and MYNN-J, the maximum $v_{10\text{m}}$ is about $2\text{ m}\cdot\text{s}^{-1}$ weaker than in the observation in large areas on the right side of the track, whereas on the left side of the track it is up to about $4\text{ m}\cdot\text{s}^{-1}$ stronger than in the observation. The maximum $v_{10\text{m}}$ on the right side of the track further inland in YSU-J is about $2\text{ m}\cdot\text{s}^{-1}$ stronger than in MYNN-J. This reflects the stronger inner core $v_{10\text{m}}$

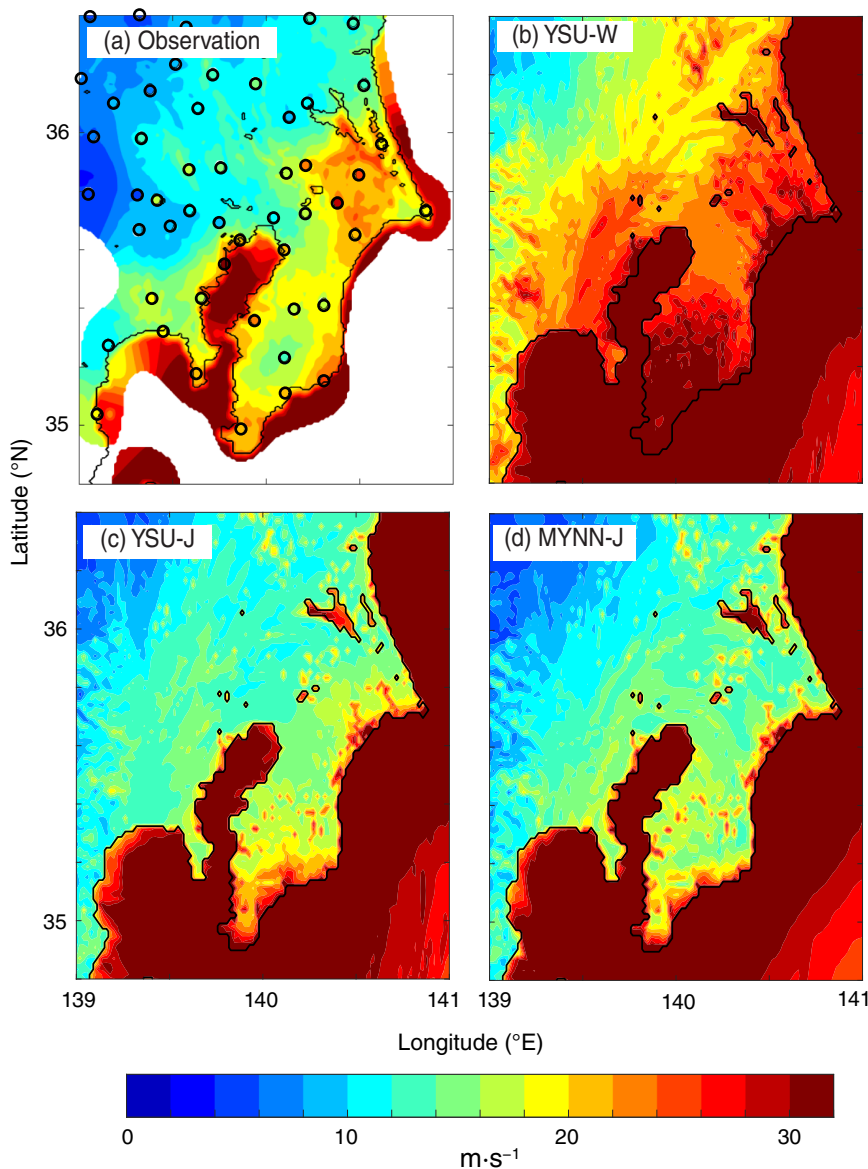


FIGURE 14 (a) The observed wind swath (the map of the maximum surface 10-min winds) in the Kanto region during the landfall of Typhoon *Faxai*. The maximum wind speeds recorded at Automated Meteorological Data Acquisition System stations are shown inside the black circles. The details for the wind swath analysis are presented in Takahashi and Nolan (2023, appendix B). (b–d) The same as (a) but for (b) Yonsei University (YSU)-W, (c) YSU-J, and (d) Mellor–Yamada–Nakanishi–Niino (MYNN)-J (W: WRF default roughness length; J: Japan Meteorological Agency’s non-hydrostatic model roughness length). [Colour figure can be viewed at wileyonlinelibrary.com]

in YSU-J than in MYNN-J, as clearly seen in the winds at stations P7, P10, and P11.

Overall, the discrepancy between the observed and simulated maximum v_{10m} is greatly reduced by increasing the surface roughness length. However, in a large area on the right side of *Faxai*’s track, maximum v_{10m} in both YSU-J and MYNN-J underestimate the observed maximum v_{10m} by a few meters per second. In particular, in the area to the south of Kasumigaura Bay (the lake north of Narita Airport), the observed v_{10m} exceeds $20 \text{ m}\cdot\text{s}^{-1}$, whereas the simulated maximum v_{10m} is only about $15 \text{ m}\cdot\text{s}^{-1}$. The time evolution of v_{10m} at some AMeDAS stations, such as Ryugasaki (P9) and Katori (P10), illustrates such large discrepancies between observed and simulated maximum v_{10m} . In Part I, we discussed that the observed strong surface winds to the south of Kasumigaura Bay are likely a result of a relatively small z_0 over areas used

for paddy fields or a mixture of paddy fields, farm fields, forests, and buildings. In the WRF simulations, a significant portion of these areas is simply represented as buildings or forests, leading to an overestimation of z_0 in YSU-J and MYNN-J. This clearly shows the crucial importance of precise representation of z_0 for accurate forecasts of surface winds.

3.5 | Size of the vortex and thickness of the inflow layer

Across the simulations, the size of the inner core of *Faxai* is larger than observed. Additionally, the simulations overestimate the height of the PBL jet associated with the eyewall over Narita Airport. This overestimation is shown to contribute to the underestimation of the peak surface winds observed during the passage of the eyewall. In this section,

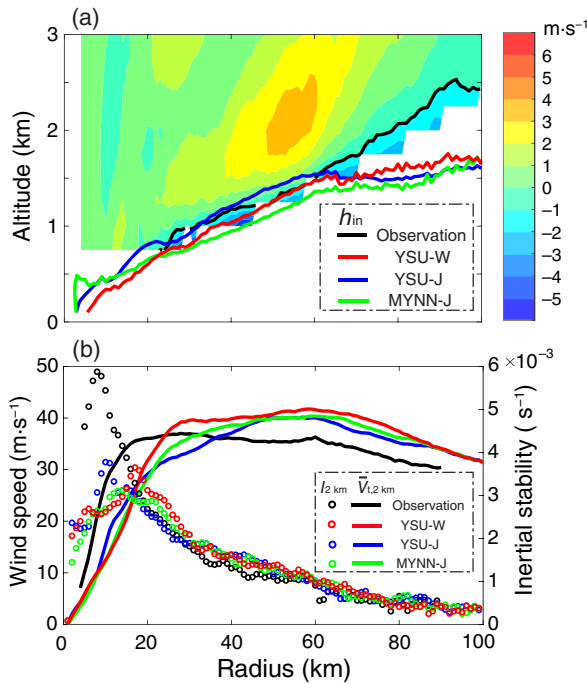


FIGURE 15 (a) The observed axisymmetric radial wind field \bar{V}_r based on the dual-Doppler analysis at 2005 UTC on September 8, together with the observed and simulated height of the inflow layer top h_{in} . (b) The observed and simulated radial profile of $\bar{V}_{t,2km}$ (solid lines) and the inertial stability at 2 km I_{2km} (open circles). YSU: Yonsei University; MYNN: Mellor–Yamada–Nakanishi–Niino; W: WRF default roughness length; J: Japan Meteorological Agency’s non-hydrostatic model roughness length. [Colour figure can be viewed at wileyonlinelibrary.com]

we compare the simulated and observed radial distribution of the height of the inflow layer top, as well as the inertial stability, and discuss the dynamical cause for the overestimation of the inner core PBL jet height h_{jet} in the simulations based on axisymmetric dynamics.

The dual-Doppler analysis does not cover the lower PBL, including the location of the PBL jet during *Faxai*. However, the top of the inflow layer outside the radius $r \sim 20$ km was observed shortly after landfall when the three radars were positioned at nearly equal distances from the center of *Faxai*. Figure 15a shows the axisymmetric radial wind \bar{V}_r at 2005 UTC on September 8 based on the dual-Doppler analysis (color shading), along with the observed and simulated height of the inflow layer top h_{in} (solid lines). Here, h_{in} is defined as the altitude where \bar{V}_r becomes -1 m s^{-1} .

Figure 15a shows that both the observed and simulated thickness of the inflow layer increases with radius. A strong outflow is observed just above the PBL around $r \sim 50$ km. The simulations underestimate h_{in} outside the rain band at $r \simeq 60$ km. Between $r \simeq 60$ km and $r \simeq 25$ km, the simulated h_{in} agrees reasonably well with the observed

h_{in} . Inside $r \simeq 60$ km, h_{in} for YSU-J is slightly higher than that for YSU-W. This is likely due to the larger eddy diffusivity $K_{m,YSU}$ in YSU-J compared with YSU-W. $K_{m,YSU}$ is proportional to the velocity scale $w_s \sim u_*$ (u_* : surface friction velocity), which in turn is enhanced in YSU-J due to the larger z_0 . h_{in} in MYNN-J is slightly lower than in YSU-J outside $r \simeq 10$ km. Figure 15a also indicates that h_{in} in reality is less than 0.7 km inside $r \simeq 20$ km. We note that YSU-J overestimates h_{in} around $r \simeq 20$ km. From the observational analysis reported by Ikuta et al. (2023), based on the radius height indicator scan of the Narita Airport radar, the thickness of the inflow layer just before *Faxai*’s landfall at 1920 UTC was approximately 0.6 km at $r \simeq 20$ km and decreased towards the center. Their observations also support the likely overestimation of h_{in} inside $r \simeq 20$ km in both YSU-J and MYNN-J.

Observational studies have revealed that the PBL jet in hurricanes over the ocean is located right below the inflow layer top (e.g., Zhang et al., 2011a). According to the linear theory of TCBL (Eliassen & Lystad, 1977; Kepert, 2001), the depth of the TCBL scales as $\delta_0 = \sqrt{2K/I}$, where K is the eddy diffusivity and I is the inertial stability. The inertial stability I is defined by $I^2 = (f + 2V/r)(f + V/r + \partial V/\partial r)$, where V is the gradient wind speed and f is the Coriolis parameter. The observed increase of h_{in} with radius in *Faxai* is consistent with both the over-ocean TCBL observation and the linear theory. We note that the linear theory of the TCBL should be considered only as a first-order approximation for landfalling TCs, given the strong non-linearity and rapid decay of the vortex. Based on the linear theory of Kepert (2001), h_{in} and h_{jet} are expressed as follows:

$$h_{in} = \delta_0 \arctan\left(-\frac{1}{1 + \chi}\right), \quad (10)$$

$$h_{jet} = \delta_0 \arctan\left(-1 - \frac{2}{\chi}\right). \quad (11)$$

Here, χ is defined by $\chi = C_d V \sqrt{2/KI}$, where C_d is the drag coefficient. With typical values for strong TCs over land (e.g., Zhang et al., 2011b), χ exceeds 1, and h_{in} and h_{jet} are approximately expressed as follows:

$$h_{jet} \simeq 0.7h_{in} \simeq 2\delta_0. \quad (12)$$

The observed low-lying PBL jet near the center of *Faxai* aligns with the aforementioned discussion based on the linear theory due mainly to the strong inertial stability near the center. Figure 15b shows the radial distribution of the observed and simulated $\bar{V}_{t,2km}$ and the inertial stability at 2 km height I_{2km} . Outside $r \simeq 20$ km, I_{2km} in all simulations agrees with observation. However, inside $r \simeq 20$ km, the simulations underestimate I_{2km} by a factor of 2. This

suggests that the overestimation of the simulated inner core PBL jet height in both YSU-J and MYNN-J is caused by the overly thick inner core PBL due to the underestimation of the inertial stability associated with the excessively large inner core size.

4 | SUMMARY

We presented a comprehensive evaluation of (1) the vortex structure, (2) PBL wind profile, and (3) near-surface winds in WRF simulations of Typhoon *Faxai* (2019) through comparative analysis with the observations presented in Part I.

To explore the impacts of the surface roughness z_0 parametrizations on vortex structure, PBL wind profile, and near-surface winds in WRF simulation, we compared two WRF simulations of *Faxai* (YSU-W and YSU-J) with different z_0 tables. YSU-W used the default z_0 table available with WRF, whereas YSU-J used larger z_0 values for urban/residential areas and forests based on climatological values from the JMA's non-hydrostatic model.

The track and intensity of *Faxai* in both YSU-W and YSU-J agreed very well with the observations during landfall. However, the size of the simulated inner core, as seen in both radar reflectivity and wind fields at 2 km height in all simulations, was larger than observed. The observed two distinct $v_{2\text{km}}$ peaks associated with the eyewall and the inner rain band were reproduced in both simulations. The simulated $v_{2\text{km}}$ peak associated with the inner rain band was stronger than observed, whereas the $v_{2\text{km}}$ peak associated with the eyewall in YSU-J was substantially weaker than observed due to the fast decay of the inner core in YSU-J over land.

The surface winds, $v_{10\text{m}}$, in YSU-W significantly overestimated the observations, indicating that the WRF default z_0 was too small. The overestimation of $v_{10\text{m}}$ in YSU-W was dramatically improved in YSU-J. However, it was shown that at many AMEDAS stations the maximum $v_{10\text{m}}$ in YSU-J underestimated observations, mainly due to the underestimation of the peak wind reduction factor $F_{2\text{km}}$ when the observed $v_{10\text{m}}$ took its maximum during the passage of the eyewall. The underestimation of $F_{2\text{km}}$ is due to the simulated eyewall PBL jet being located too high, as revealed by the comparative analysis over Narita Airport. In addition, YSU-J significantly underestimated the maximum $v_{10\text{m}}$ over the area south of Kasumigaura Bay, where the land is used for paddy fields or a mixture of paddy fields, farm fields, forests, and buildings.

Also, the impacts of the PBL parametrizations on vortex structure, PBL wind profile, and near-surface winds in WRF simulation were explored based on the comparison of three WRF simulations of *Faxai* (YSU-J,

MYJ-J, and MYNN-J) with different PBL parametrizations; namely, YSU, MYJ, and MYNN schemes using the enhanced z_0 table. The simulated intensity of *Faxai* at landfall in YSU-J and MYNN-J agreed well with the best track, whereas that in MYJ-J was weaker. The main differences in the axisymmetric vortex structure between YSU-J and MYNN-J were as follows. First, the inner core of *Faxai* in YSU-J was more compact than in MYNN-J at 2 km height, as seen both in reflectivity and wind fields; second, the PBL depth, as seen in the inflow layer top h_{in} , in YSU-J is located higher than in MYNN-J outside $r \simeq 20$ km, whereas it is lower than in MYNN-J near the center.

Radar observations suggest that both YSU-J and MYNN-J overestimate the PBL depth near the center. Based on the linear theory of TCBL (Kepert, 2001), the likely overestimation of the inner core PBL jet height in the simulations was attributed to the significant underestimation of the inertial stability due to the excessively large inner core.

In conclusion, it was shown that surface roughness parametrization has a significant impact on both the vortex structure and near-surface winds during landfall. In addition, the choice of PBL parametrizations is found to impact the surface winds through the control of the vortex size and the PBL jet height.

AUTHOR CONTRIBUTIONS

Takuya Takahashi: conceptualization; formal analysis; methodology; writing – original draft. **David S. Nolan:** conceptualization; funding acquisition; supervision; writing – review and editing. **Brian D. McNoldy:** software; writing – review and editing.

ACKNOWLEDGEMENTS

We thank S. Majumdar, J. Zhang, and T. Aoyagi for their valuable comments. We also thank X. Chen for kindly providing us with the revised MYNN PBL code tailored for hurricane conditions for use in our WRF simulations. Additionally, our thanks go to C. Landsea and M. DeMaria for their constructive reviews. The WRF simulations used in this study were produced and are archived at the University of Miami Institute for Data Sciences and Computing (IDSC). D. Nolan and B. McNoldy were supported by the National Science Foundation under the Prediction of and Resilience Against Extreme Events (PREEVENTS) program, Award ICER-1663947.

DATA AVAILABILITY STATEMENT

The data that support the findings of this study are available from the corresponding author upon reasonable request.

ORCID

Takuya Takahashi  <https://orcid.org/0009-0007-3706-746X>

David S. Nolan  <https://orcid.org/0000-0003-0183-056X>

Brian D. McNoldy  <https://orcid.org/0000-0003-0217-1025>

REFERENCES

- Alford, A.A., Zhang, J.A., Biggerstaff, M.I., Dodge, P., Marks, F.D. & Bodine, D.J. (2020) Transition of the hurricane boundary layer during the landfall of hurricane Irene (2011). *Journal of the Atmospheric Sciences*, 77, 3509–3531.
- Aoyagi, T. & Seino, N. (2012) A mesoscale numerical forecasting model in urban area. *Meteorological Research Note*, 224, 273–301 (in Japanese).
- Biggerstaff, M.I., Alford, A.A., Stevenson, J.A. & Carrie, G.D. (2021) Hurricane Florence (2018): long duration single- and dual-Doppler observations and wind retrievals during landfall. *Geoscience Data Journal*, 9, 273–287.
- Blackadar, A.K. (1962) The vertical distribution of wind and turbulent exchange in neutral atmosphere. *Journal of Geophysical Research*, 67, 3095–3102.
- Bougeault, P. & Lacarrere, P. (1989) Parameterization of orography-induced turbulence in a mesobeta-scale model. *Monthly Weather Review*, 117, 1872–1890.
- Cha, T.-Y. & Bell, M.M. (2021) Comparison of single-Doppler and multiple-Doppler wind retrievals in hurricane Matthew (2016). *Atmospheric Measurement Techniques*, 14, 3523–3539.
- Charnock, H. (1955) Wind stress on a water surface. *Quarterly Journal of the Royal Meteorological Society*, 81, 639–640.
- Chen, J. & Chavas, D.R. (2020) The transient responses of an axisymmetric tropical cyclone to instantaneous surface roughening and drying. *Journal of the Atmospheric Sciences*, 77, 2807–2834.
- Chen, J. & Chavas, D.R. (2021) Can existing theory predict the response of tropical cyclone intensity to idealized landfall? *Journal of the Atmospheric Sciences*, 78, 3281–3296.
- Chen, X. & Bryan, G.H. (2021) Role of advection of parameterized turbulence kinetic energy in idealized tropical cyclone simulations. *Journal of the Atmospheric Sciences*, 78, 3593–3611.
- Curcic, M. & Haus, B.K. (2020) Revised estimates of ocean surface drag in strong winds. *Geophysical Research Letters*, 47, e2020GL087647.
- Deng, A., Stauffer, D.R., Dudhia, J., Otte, T.L. & Hunter, G.K. (2007) Update on analysis nudging FDDA in WRF-ARW. Eighth WRF Users' Workshop, Boulder, CO, WRF, 4, 8.
- Donelan, M.A., Haus, B.K., Reul, N., Plant, W.J., Stiassne, M., Graber, H.C. et al. (2004) On the limiting aerodynamic roughness of the ocean in very strong winds. *Geophysical Research Letters*, 31, L18306.
- Dvorak, V.F. (1975) Tropical cyclone intensity analysis and forecasting from satellite imagery. *Monthly Weather Review*, 103, 420–430.
- Dvorak, V.F. (1984) Tropical cyclone intensity analysis using satellite data. *NOAA Technical Report*, 11, 45.
- Eliassen, A. & Lystad, M. (1977) The Ekman layer of a circular vortex: a numerical and theoretical study. *Geophysica Norvegica*, 31, 1–16.
- Emanuel, K.A. (1986) An air-sea interaction theory for tropical cyclones. Part I: steady-state maintenance. *Journal of the Atmospheric Sciences*, 43, 585–604.
- Fierro, A.O., Rogers, R.F., Marks, F.D. & Nolan, D.S. (2009) The impact of horizontal grid spacing on the microphysical and kinematic structures of strong tropical cyclones simulated with the WRF-ARW model. *Monthly Weather Review*, 137, 3717–3743.
- Franklin, J.L., Black, M.L. & Valde, K. (2003) GPS dropwindsonde wind profiles in hurricanes and their operational implications. *Weather Forecasting*, 18, 32–44.
- Gopalakrishnan, S.G., Marks, F., Zhang, X., Bao, J.-W., Yeh, K.-S. & Atlas, R. (2011) The experimental HWRF system: a study on the influence of horizontal resolution on the structure and intensity changes in tropical cyclones using an idealized framework. *Monthly Weather Review*, 139, 1762–1784.
- Harper, B.A., Kepert, J.D. & Ginger, J.D. (2010) Guidelines for converting between various wind averaging periods in tropical cyclone conditions. World Meteorological Organization tech. Doc. WMO/TD-1555, 54.
- Hendricks, E.A., Kniviel, J.C. & Nolan, D.S. (2021) Evaluation of boundary layer and urban canopy parameterizations for simulating wind in Miami during hurricane Irma (2017). *Monthly Weather Review*, 149, 2321–2349.
- Hlywiak, J. & Nolan, D.S. (2021) The response of the near-surface tropical cyclone wind field to inland surface roughness length and soil moisture content during and after landfall. *Journal of the Atmospheric Sciences*, 78, 983–1000.
- Hong, S.-Y., Noh, Y. & Dudhia, J. (2006) A new vertical diffusion package with an explicit treatment of entrainment processes. *Monthly Weather Review*, 134, 2318–2341.
- Hong, S.-Y. & Pan, H.-L. (1996) Nonlocal boundary layer diffusion in a medium-range forecast model. *Monthly Weather Review*, 124, 2322–2339.
- Ikuta, Y., Sawada, M. & Satoh, M. (2023) Determining the impact of boundary layer schemes on the secondary circulation of typhoon FAXAI using radar observations in the gray zone. *Journal of the Atmospheric Sciences*, 80, 961–981.
- Janjić, Z.I. (1990) The step-mountain coordinate: physical package. *Monthly Weather Review*, 118, 1429–1443.
- Janjić, Z.I. (1994) The step-mountain eta coordinate model: further developments of the convection, viscous sublayer, and turbulence closure schemes. *Monthly Weather Review*, 122, 927–945.
- Janjić, Z.I. (2002) Nonsingular implementation of the Mellor-Yamada level 2.5 scheme in the NCEP Meso model. *NCEP Office Note*, 437, 61.
- Kanada, S. & Wada, A. (2016) Sensitivity to horizontal resolution of the simulated intensifying rate and inner-core structure of typhoon ida, an extremely intense typhoon. *Journal of the Meteorological Society of Japan*, 94A, 181–190.
- Kepert, J.D. (2001) The dynamics of boundary layer jets within the tropical cyclone core. Part I: linear theory. *Journal of the Atmospheric Sciences*, 58, 2469–2484.
- Kepert, J.D. (2012) Choosing a boundary-layer parameterization for tropical cyclone modeling. *Monthly Weather Review*, 140, 1427–1445.
- Kepert, J.D. & Wang, Y. (2001) The dynamics of boundary layer jets within the tropical cyclone core. Part II: nonlinear enhancement. *Journal of the Atmospheric Sciences*, 58, 2485–2501.
- Koba, H., Hagiwara, T., Osano, S. & Akashi, S. (1990) Relationships between CI number from Dvorak's technique and minimum sea level pressure or maximum wind speed of tropical cyclone. *Journal of Meteorological Research*, 42, 59–67 (in Japanese).

- Kosiba, K., Wurman, J., Masters, F.J. & Robinson, P. (2013) Mapping of near-surface winds in hurricane Rita using finescale radar, anemometer, and land-use data. *Monthly Weather Review*, 141(12), 4337–4349.
- Kurihara, Y.M., Bender, M.A. & Ross, R.J. (1993) An initialization scheme of hurricane models by vortex specification. *Monthly Weather Review*, 121, 2030–2045.
- Kurihara, Y.M., Bender, M.A., Tuleya, R.E. & Ross, R.J. (1995) Improvements in the GFDL hurricane prediction system. *Monthly Weather Review*, 123, 2791–2801.
- Kuwagata and Kondo. (1992) Surface wind field analysis of the 9119 typhoon using roughness correction wind data. *Journal of Jsnads*, 11-2, 87–96.
- Lee, W.-C., Jou, B.J.-D., Chang, P.-L. & Marks, F.D. (2000) Tropical cyclone kinematic structure retrieved from single-Doppler radar observations. Part III: evolution and structures of typhoon Alex (1987). *Monthly Weather Review*, 128, 3982–4001.
- Li, X. & Pu, Z. (2021) Vertical eddy diffusivity parameterization based on a large-eddy simulation and its impact on prediction of hurricane landfall. *Geophysical Research Letters*, 48, e2020GL090703.
- Lim, K.-S.S. & Hong, S.-Y. (2010) Development of an effective double-moment cloud microphysics scheme with prognostic cloud condensation nuclei (CCN) for weather and climate models. *Monthly Weather Review*, 138, 1587–1612.
- Lin, N., Smith, J.A., Villarini, G., Marchok, T.P. & Lynn, M. (2010) Modeling extreme rainfall, winds, and surge from hurricane Isabel (2003). *Weather Forecasting*, 25, 1342–1361.
- Mashiko, W. (2008) Formation mechanism of a low-level jet during the passage of typhoon Ma-on (2004) over the southern Kanto District. *Journal of the Meteorological Society of Japan*, 86, 183–202.
- Mason, P.J. & Thomson, D.J. (1992) Stochastic backscatter in large-eddy simulations of boundary layers. *Journal of Fluid Mechanics*, 242, 51–78.
- Mellor, G.L. & Yamada, T. (1974) A hierarchy of turbulence closure models for planetary boundary layers. *Journal of the Atmospheric Sciences*, 31, 1791–1806.
- Mellor, G.L. & Yamada, T. (1982) Development of a turbulence closure model for geophysical fluid problems. *Reviews of Geophysics*, 20, 851–875.
- Monin, A.S. & Obukhov, A.M. (1954) Basic laws of turbulent mixing in the surface layer of the atmosphere. *Contributions of the Geophysical Institute of the Slovak Academy of Sciences Ussr*, 151, 163–187 (in Russian).
- Moon, Y. & Nolan, D.S. (2010) The dynamic response of the hurricane wind field to spiral rainband heating. *Journal of the Atmospheric Sciences*, 67, 1779–1805.
- Nakanishi, M. (2001) Improvement of the Mellor-Yamada turbulence closure model based on large-eddy simulation data. *Boundary-Layer Meteorology*, 99, 349–378.
- Nakanishi, M. & Niino, H. (2009) Development of an improved turbulence closure model for the atmospheric boundary layer. *Journal of the Meteorological Society of Japan*, 87, 895–912.
- Nakazawa, T. & Hoshino, S. (2009) Intercomparison of Dvorak parameters in tropical cyclone datasets over the western North Pacific. *Scientific Online Letters on the Atmosphere*, 5, 33–36.
- Nguyen, L.T., Molinari, J. & Thomas, D. (2014) Evaluation of tropical cyclone center identification methods in numerical models. *Monthly Weather Review*, 142, 4326–4339.
- Nolan, D.S., Atlas, R., Bhatia, K.T. & Bucci, L.R. (2013) Development and validation of a hurricane nature run using the joint OSSE nature run and the WRF model. *Journal of Advances in Modeling Earth Systems*, 5, 382–405.
- Nolan, D.S., McNoldy, B.D. & Yunge, J. (2021a) Evaluation of the surface wind field over land in WRF simulations of hurricane Wilma (2005). Part I: model initialization and simulation validation. *Monthly Weather Review*, 149, 679–695.
- Nolan, D.S., McNoldy, B.D., Yunge, J., Masters, F.J. & Giammanco, I.M. (2021b) Evaluation of the surface wind field over land in WRF simulations of hurricane Wilma (2005). Part II: surface winds, inflow angles, and boundary layer profiles. *Monthly Weather Review*, 149, 697–713.
- Nolan, D.S., Stern, D.P. & Zhang, J.A. (2009b) Evaluation of planetary boundary layer parameterizations in tropical cyclones by comparison of in situ observations and high-resolution simulations of hurricane Isabel (2003). Part II: inner-core boundary layer and eyewall structure. *Monthly Weather Review*, 137, 3675–3698.
- Nolan, D.S., Zhang, J.A. & Stern, D.P. (2009a) Evaluation of planetary boundary layer parameterizations in tropical cyclones by comparison of in situ observations and high-resolution simulations of hurricane Isabel (2003). Part I: initialization, maximum winds, and the outer-core boundary layer. *Monthly Weather Review*, 137, 3651–3674.
- Nolan, D.S., Zhang, J.A. & Uhlhorn, E.W. (2014) On the limits of estimating the maximum wind speeds in hurricanes. *Monthly Weather Review*, 142, 2814–2837.
- Olson, J.B., Kenyon, J.S., Angevine, W.M., Brown, J.M., Pagowski, M. & Sušelj, K. (2019) A description of the MYNN-EDMF scheme and coupling to other components in WRF-ARW. *NOAA Tech. Memo. OARGSD*, 61, 37.
- Powell, M.D. (1982) The transition of the hurricane Frederic boundary layer wind fields from the open Gulf of Mexico to landfall. *Monthly Weather Review*, 110, 1912–1932.
- Prandtl, L. (1925) Bericht über Untersuchungen zur ausgebildeten Turbulenz. *Zeitschrift für Angewandte Mathematik Und Mechanik*, 5(1), 136–139.
- Rappin, E.D., Nolan, D.S. & Majumdar, S.J. (2013) A highly configurable vortex initialization method for tropical cyclones. *Monthly Weather Review*, 141, 3556–3575.
- Rotunno, R., Chen, Y., Wang, W., Davis, C., Dudhia, J. & Holland, G.J. (2009) Large-eddy simulation of an idealized tropical cyclone. *Bulletin of the American Meteorological Society*, 90, 1783–1788.
- Shapiro, L.J. (1983) The asymmetric boundary layer under a translating hurricane. *Journal of the Atmospheric Sciences*, 40, 1984–1998.
- Shimada, U., Sawada, M. & Yamada, H. (2018) Doppler radar analysis of the rapid intensification of typhoon Goni (2015) after eyewall replacement. *Journal of the Atmospheric Sciences*, 75, 143–162.
- Skamarock, W.C. (2019) A description of the advanced research WRF model version 4. NCAR Tech. Note. NCAR/TN-556+STR, 145.
- Smith, R.K. & Montgomery, M.T. (2013) On the existence of the logarithmic surface layer in the inner core of hurricanes. *Quarterly Journal of the Royal Meteorological Society*, 140, 72–81.
- Smith, R.K. & Vogl, S. (2008) A simple model of the hurricane boundary layer revisited. *Quarterly Journal of the Royal Meteorological Society*, 134, 337–351.

- Sroka, S. & Emanuel, K. (2021) A review of parameterizations for enthalpy and momentum fluxes from sea spray in tropical cyclones. *Journal of Physical Oceanography*, 51, 3053–3069.
- Stern, D.P., Bryan, G.H., Lee, C.-Y. & Doyle, J.D. (2021) Estimating the risk of extreme wind gusts in tropical cyclones using idealized large-eddy simulations and a statistical-dynamical model. *Monthly Weather Review*, 149, 4183–4204.
- Takahashi, T. & Nolan, D.S. (2023) The vortex structure and near-surface winds of typhoon Faxai (2019) during landfall. Part I. Observational analysis. *Quarterly Journal of the Royal Meteorological Society*, 22, qj4641. Available from: <https://doi.org/10.1002/qj4641>
- Thompson, G., Field, P.R., Rasmussen, R.M. & Hall, W.D. (2008) Explicit forecasts of winter precipitation using an improved bulk microphysics scheme. Part II: implementation of a new snow parameterization. *Monthly Weather Review*, 136, 5095–5115.
- Vickery, P.J., Masters, F.J., Powell, M.D. & Wadhera, D. (2009) A hurricane boundary layer and wind field model for use in engineering applications. *Journal of Applied Meteorology and Climatology*, 48, 381–405.
- Wadler, J.B., Nolan, D.S., Zhang, J.A., Shay, L.K., Olson, J.B. & Cione, J.J. (2023) The effect of advection on the three-dimensional distribution of turbulent kinetic energy and its generation in idealized tropical cyclone simulations. *Journal of Advances in Modeling Earth Systems*, 15(5), e2022MS003230.
- Wu, C.-C., Cheng, H.-J., Wang, Y. & Chou, K.-H. (2009) A numerical investigation of the eyewall evolution of a landfalling typhoon. *Monthly Weather Review*, 137, 21–40.
- Zhang, J.A., Nolan, D.S., Rogers, R.F. & Tallapragada, V. (2015) Evaluating the impact of improvements in the boundary layer parameterizations on hurricane intensity and structure forecasts in HWRF. *Monthly Weather Review*, 143, 3136–3155.
- Zhang, J.A., Rogers, R.F., Nolan, D.S. & Marks, F.D. (2011a) On the characteristic height scales of the hurricane boundary layer. *Monthly Weather Review*, 139, 2523–2535.
- Zhang, J.A., Zhu, P., Masters, F.J., Rogers, R.F. & Marks, F.D. (2011b) On momentum transport and dissipative heating during hurricane landfalls. *Journal of the Atmospheric Sciences*, 68, 1397–1404.

How to cite this article: Takahashi, T., Nolan, D.S. & McNoldy, B.D. (2024) The vortex structure and near-surface winds of Typhoon Faxai (2019) during landfall. Part II: Evaluation of WRF simulations. *Quarterly Journal of the Royal Meteorological Society*, 1–25. Available from: <https://doi.org/10.1002/qj.4663>